Beamformer Design and Optimization for Joint Communication and Full-Duplex Sensing at mm-Waves

Carlos Baquero Barneto, *Student Member, IEEE*, Taneli Riihonen, *Senior Member, IEEE*,
Sahan Damith Liyanaarachchi, *Graduate Student Member, IEEE*, Mikko Heino, *Member, IEEE*,
Nuria González-Prelcic, *Senior Member, IEEE*, and Mikko Valkama, *Fellow, IEEE*

Abstract—In this article, we study the joint communication and sensing (JCAS) paradigm in the context of millimeter-wave (mm-wave) mobile communication networks. We specifically address the JCAS challenges stemming from the full-duplex operation in monostatic orthogonal frequency-division multiplexing (OFDM) radars and from the co-existence of multiple simultaneous beams for communications and sensing purposes. To this end, we first formulate and solve beamforming optimization problems for hybrid beamforming based multiuser multiple-input and multiple-output JCAS systems. The cost function to be maximized is the beamformed power at the sensing direction while constraining the beamformed power at the communications directions, suppressing interuser interference and cancelling full-duplexing related self-interference (SI). We then also propose new transmitter and receiver beamforming solutions for purely analog beamforming based JCAS systems that maximize the beamforming gain at the sensing direction while controlling the beamformed power at the communications direction(s), cancelling the SI as well as eliminating the potential reflection from the communication direction and optimizing the combined radar pattern (CRP). Both closed-form and numerical optimization based formulations are provided. We analyze and evaluate the performance through extensive numerical experiments, and show that substantial gains and benefits in terms of radar transmit gain, CRP, and SI suppression can be achieved with the proposed beamforming methods.

Index Terms—Beamforming, full-duplex, joint communication and sensing, mm-wave, monostatic radar, self-interference.

I. INTRODUCTION

JOINT communication and sensing (JCAS) technology is experiencing a rapidly growing interest in both defense and civilian application domains, in response to the increasingly congested electromagnetic spectrum [1]. Another driving factor is the evolution of the wireless communication networks to higher frequency bands, where larger channel bandwidths and directional antenna systems allow for extracting accurate positioning and sensing information [1], [2]. In general, there are three main research areas reflecting different levels of convergence between the communication and radar/sensing functions or systems, namely the so-called *co-existence*, *cooperation* and *co-design* paradigms [3]. In this work, we focus on the *co-design* area, which seeks to merge the communication and sensing functionalities into the joint shared platform with common waveform and hardware [1], [3], [4], [5]. Such an approach can benefit both communications and sensing operations while relaxing the spectrum congestion, providing thus an efficient and appealing alternative compared to classical fully separated stand-alone systems [1]. Timely application fields contain, e.g., vehicular systems, unmanned aerial vehicles, residential security, building analytics and health monitoring [6], [7], [8], [9], [10], to name a few.

In the context of cellular networks, integrating efficient sensing features into the future sixth generation (6G) mobile communication networks is one research area of largely increasing importance [2], [11]. In general, the mobile networks are evolving to support operation at the so-called millimeter-wave (mm-wave) bands (30–300 GHz), with the current fifth generation (5G) New Radio (NR) specifications reaching up to 52.6 GHz [12]. It is expected that the beyond 52.6 GHz bands will also be utilized, through later 5G NR standard releases, while in the 6G-era the networks will be further expanding towards the sub-THz frequencies [2], [13], [14].

From the sensing and JCAS perspectives, the transition to the mm-wave bands exhibits great opportunities and benefits. The large bandwidths used at mm-waves enable receivers with enhanced ability to resolve the delays of the different multipath components, which results in better range estimation [15]. In addition, high frequencies and subsequently small wavelengths imply more compact antennas, which allow to deploy large amounts of antenna units and thereon implement highly directive antenna arrays even in small form-factor devices, improving the angular observation capabilities of the systems [4], [16]. Finally, propagation is also different at mm-waves and above; diffraction tends to be lower due to the reduced Fresnel zone, while scattering is higher due to the

increased effective roughness of the materials [17]. Therefore, mm-wave channels tend to have few dominant multipath components beyond a strong line-of-sight and a non-line-of-sight with a few reflections, enabling sparse channel models which are easier to relate to the propagation environment in order to obtain sensing information.

A. State-of-the-Art

In the recent literature, three main operation modes have been investigated to incorporate JCAS functionalities to wireless communication networks, such that the base station (BS) and/or the user equipment (UE) are utilized also for sensing purposes [18], [19]. The first JCAS mode is known as *downlink active sensing*, and refers to the case where a BS collects the reflections stemming from its own downlink signal. In this case, the BS operates essentially as a monostatic radar where the sensing transmitter (TX) and receiver (RX) are colocated [20]. Alternatively, the BS can be used for *downlink passive sensing* by collecting the reflections from downlink signals of different BSs, representing a passive radar scheme. Finally, the UE can be utilized for *uplink sensing*, operating as a mobile JCAS system by collecting the reflections of its own transmit signal as a monostatic device [21]. Alternatively, the UE-based uplink signals can be exploited by the neighbouring BSs for passive sensing purposes. In general, these JCAS scenarios present different requirements and various design challenges as described in [19]. One prominent research problem is the so-called joint waveform design, as the same waveform is shared between the communications and the sensing tasks. As most of the modern wireless networks are orthogonal frequency-division multiplexing (OFDM)-based, different OFDM variants and related optimization approaches have been recently studied in the JCAS context [20], [22].

The recently studied mm-wave JCAS systems build commonly on massive antenna arrays with directive patterns to compensate for the small aperture of each antenna element and to obtain directional information of the targets [17], [23]. Depending on the implementation assumptions, these can be further categorized into analog, digital and hybrid analog–digital beamforming systems. In analog beamforming JCAS systems, a single transmit stream is subject to a set of analog weights and transmitted from a single RF chain for both communication and sensing purposes [24], [25]. In contrast, with digital beamforming and multiple TX/RX chains, the JCAS platform is able to perform multiple-input and multiple-output (MIMO) communication and sensing by transmitting multiple parallel streams through several RF chains. However, purely digital beamforming based approach, where each antenna element is connected to its own RF chain, is not necessarily implementation-feasible at mm-waves due to challenges related to power consumption, costs and silicon area [17] — especially when the number of the antenna units is large. To overcome this problem, one can consider hybrid architectures where the overall MIMO beamforming task is split into the analog and digital domains. In this work, we address the design and optimization challenges of

both purely analog and hybrid analog-digital beamforming configurations in the JCAS context, as illustrated in Fig. 1.

While beamforming techniques have been extensively studied over the past decades for communications at large, some recent works have proposed new beamforming designs to meet the additional requirements stemming specifically from the JCAS operation. In [24], [25], the so-called multibeam approach using steerable analog antenna arrays was identified as one of the main enablers for mm-wave JCAS systems. The proposed multibeam scheme provides separate controllable beams for communication and sensing with different design requirements. In [26], in turn, joint TX beamforming for multiuser (MU) MIMO communications and MIMO radar was investigated. In this case, the JCAS system transmits a sum of independent communication and sensing waveforms, forming multiple beams. The effects of beamforming weight quantization in multibeam JCAS systems were analyzed in [27], focusing purely on the TX side and thus neglecting joint TX–RX optimization.

Finally, an important JCAS design and deployment challenge is related to the TX–RX isolation [3], [6], [28]. To this end, two duplexing modes can basically be considered known as half-duplex and full-duplex (FD) [29], [30]. In half-duplex sensing systems, such as ordinary pulse radars, the RX observes and collects the targets' reflections only when the TX has finalized the transmission of a sensing pulse. Therefore, the TX and RX never operate simultaneously, ensuring thus automatically high TX–RX isolation. However, such approach is not feasible for JCAS in wireless communication networks, where the transmit waveform is by default imposed by the communication requirements and the corresponding system specifications [22], [31], [32], [33]. As a consequence, FD operation is required implying a simultaneous transmit-and-receive (STAR) mode [34] — even in time-division duplexing (TDD) based networks, when viewed from the sensing function's point of view. Thus, one major technical challenge is the self-interference (SI) between TX and RX, which requires SI cancellation (SIC) to provide sufficient TX–RX isolation [35]. This is one of the JCAS challenges addressed in this article, through the beamforming design and optimization, with specific focus on monostatic OFDM radar configuration where the SI challenge is the most substantial [6], [20]. This is particularly so with high-power macro base-stations where the effective isotropic radiated powers (EIRP) can extend towards the $+70 \ldots +100$ dBm range.

B. Contributions, Novelty, and Organization

In this article, we propose multiple new beamforming design and optimization solutions for full-duplex based mm-wave JCAS systems. We cover both analog array and hybrid MU-MIMO based JCAS scenarios, and propose novel TX and RX beamforming solutions to address particularly the challenges related to (*i*) SI stemming from the STAR operation and (*ii*) the co-existence and interference between the simultaneous communication and sensing beams. As a fundamental basis, we first provide comprehensive JCAS system

(a) Analog beamforming JCAS architecture

(b) Hybrid beamforming MU-MIMO JCAS architecture
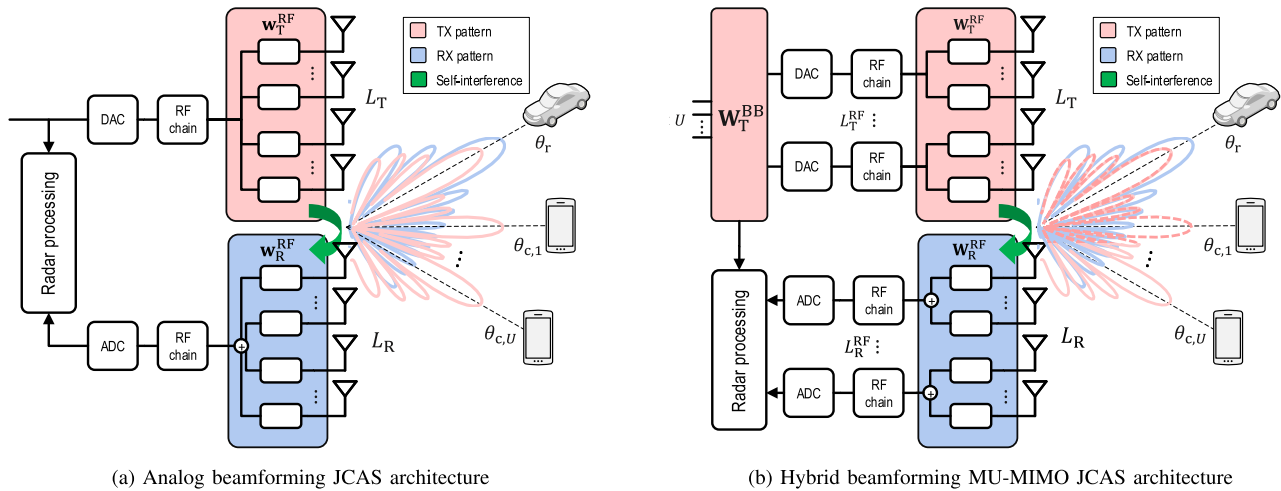
Fig. 1. Considered JCAS beamforming architectures with multiple communication beams for U users at directions $\boldsymbol{\theta}_c = [\theta_{c,1}, \ldots, \theta_{c,U}]^T$ while simultaneously sensing the environment with a directional beam at θ_r. Specifically, (a) illustrates the considered analog array based JCAS architecture while (b) shows the corresponding hybrid MU-MIMO JCAS architecture.

models for OFDM-based networks, describing how TX and RX beamformer weights, beamforming architectures, multiple simultaneous beams, multiple targets and the SI contribute to the observed signal at sensing RX. In addition, gain pattern models are also derived, that together with the received signal models form the basis for the beamforming optimization. To this end, with focus on monostatic OFDM radars, the main technical contributions and scientific novelty of this article can be summarized as follows:

- We formulate and solve TX and RX beamforming optimization problems for hybrid MU-MIMO JCAS systems that maximize the beamformed power at the sensing direction while constraining the beamformed power at the communication directions, suppress interuser interference (IUI) and cancel SI in a controlled manner.
- We propose new TX and RX analog beamforming solutions for JCAS systems, in both closed-form and numerical optimization based formulations, which simultaneously provide multiple beams for communications and sensing, suppress the SI and cancel the undesired reflections stemming from the communication beams by optimizing the so-called combined radar pattern (CRP).
- The performance of the proposed methods is assessed and mutually compared through comprehensive numerical experiments, demonstrating that substantial gains and benefits can be achieved, in terms of radar TX gain, CRP and SI suppression, compared to the existing reference approaches.

The rest of this article is organized as follows: Section II develops the fundamental system models. Sections III and IV present the proposed TX and RX beamforming solutions for the hybrid beamforming MU-MIMO and analog beamforming JCAS scenarios, respectively. Section V provides a vast collection of numerical results and their analysis, while Section VI summarizes the conclusions.

Notations: Vectors are denoted by bold lowercase letters (i.e., $\mathbf{a}$), bold uppercase letters are used for matrices

(i.e., $\mathbf{A}$) and scalars are denoted by normal font (i.e., a). The operators $(\cdot)^T$, $(\cdot)^*$, $(\cdot)^H$, $(\cdot)^\dagger$, $\mathbb{E}\{\cdot\}$, $|\cdot|$ and $\|\cdot\|$ denote the transpose, conjugate, Hermitian transpose, pseudoinverse, expectation, absolute value and Euclidian norm, respectively.

II. SYSTEM MODEL

In this section, we formulate the fundamental signal and system models for the JCAS transceiver architectures depicted in Fig. 1. Both analog beamforming (ABF) and hybrid beamforming (HBF) architectures are considered, as illustrated in the figure. Furthermore, from the communications point of view, a half-duplex TDD-based network is assumed, hence the full-duplex capability is utilized for measuring the target reflections while no actual received data signal is considered when transmitting.

A. Basic Assumptions and Notations

The JCAS system is assumed to provide one sensing/radar beam at direction θ_r and U communication beams at directions $\boldsymbol{\theta}_c = [\theta_{c,1}, \ldots, \theta_{c,U}]^T$. The sensing beam direction θ_r is a quantity which controls the illumination direction of the radar functionality, and can be varied over time. We further assume that the JCAS transmitter has communication channel state information only in the form of dominant path angles of the intended communication receivers. This is very plausible and common assumption in mm-wave beamforming research [24], [25], [27], and can generally refer either to the line-of-sight directions, if such exist, or to the directions of the dominant scatterers from the receiving terminals point of view. Furthermore, to facilitate some passive physical TX–RX isolation to begin with, separate TX and RX antenna systems are assumed, as illustrated in Fig. 1. For notational and conceptual simplicity, we assume uniform linear arrays (ULAs) for both TX and RX and focus on communications and sensing in the azimuth domain. However, the same design principles can be extended and applied also for the elevation domain and

subsequently for 3D JCAS operation. The TX system is used for both communication and sensing functionalities by sharing the same TX waveform, providing multiple beams, while the colocated RX system is executed simultaneously for sensing purposes, providing a single beam in the radar direction. Due to the STAR operation and monostatic configuration, additional SI suppression is needed on top of the physical isolation, which in our work is pursued through SI channel knowledge and beamforming optimization.

The HBF JCAS architecture shown in Fig. 1(b) allows to transmit U parallel streams, one for each communication user, through spatial multiplexing [17]. The TX side is assumed to contain a total of L_T^{RF} RF chains and L_T antenna elements, respectively, with $U < L_T^{RF} < L_T$; it is further assumed that each subarray is fed by one RF chain only. On the RX side, we assume a total of L_R antenna elements, organized into subarrays and connected to L_R^{RF} RF chains, with $L_R^{RF} < L_R$. The ABF JCAS architecture shown in Fig. 1(a) contains only a single RF chain on the TX and RX sides, i.e., $L_T^{RF} = L_R^{RF} = 1$, serving all the antenna units. In this case, only a single spatial stream is feasible, however, multiple beams can still be capitalized through for example the frequency multiplexing of users in OFDM system context, meaning that different users are allocated into different subsets of subcarriers within the overall channel bandwidth.

Similar to many reference works [20], [22], [31], [32], [33], [36], OFDM is assumed as the baseline waveform. In the following, the OFDM subcarrier index is denoted by $n = 0, \ldots, N - 1$, with N referring to the number of active subcarriers, and the signal models are expressed for an arbitrary subcarrier and multicarrier symbol duration in the baseband equivalent notion. Furthermore, in HBF case, $x_{u,n}$, $u = 1, \ldots, U$, denote the U spatially multiplexed symbols at subcarrier n. In the ABF case, in turn, the corresponding data symbol is denoted by x_n. For simplicity, in the following system model we assume a static channel, however, the considered OFDM-based system model can be easily extended to time-varying channels and sensing of moving targets as shown in [20], [31], [32], [33].

B. Spatial TX Signals

Considering first the HBF JCAS architecture, the beamformed spatial TX signal samples at subcarrier n and within an arbitrary OFDM symbol index can be expressed as

$$\tilde{\mathbf{x}}_n^{HBF} = \mathbf{W}_T^{RF} \sum_{u=1}^{U} \mathbf{w}_{T,u,n}^{BB} x_{u,n}, \tag{1}$$

where $\mathbf{W}_T^{RF} \in \mathbb{C}^{L_T \times L_T^{RF}}$ and $\mathbf{w}_{T,u,n}^{BB} \in \mathbb{C}^{L_T^{RF} \times 1}$ are the TX RF weights and the frequency-dependent BB precoder weights for the uth stream, respectively, while $x_{u,n}$, $u = 1, \ldots, U$, denote the spatially multiplexed data symbols. Denoting

$$\mathbf{W}_{T,n}^{BB} = \left[\mathbf{w}_{T,1,n}^{BB}, \mathbf{w}_{T,2,n}^{BB}, \ldots, \mathbf{w}_{T,U,n}^{BB} \right], \tag{2}$$

$$\mathbf{x}_n = \left[x_{1,n}, x_{2,n}, \ldots, x_{U,n} \right]^T, \tag{3}$$

the spatial transmit signal in (1) can be rewritten in vector–matrix notation directly as

$$\tilde{\mathbf{x}}_n^{HBF} = \mathbf{W}_T^{RF} \mathbf{W}_{T,n}^{BB} \mathbf{x}_n. \tag{4}$$

TABLE I
System Model Notations and Variables

Variable	Definition	Size
L_T	Number of TX antenna elements	–
L_R	Number of RX antenna elements	–
L_T^{RF}	Number of TX RF chains	–
L_R^{RF}	Number of RX RF chains	–
U	Number of users	–
θ_r	Radar beam direction	–
$\theta_{c,u}$	Communication beam direction for u^{th} user	–
$\boldsymbol{\theta}_c$	Communication beam direction vector	$U \times 1$
$\mathbf{W}_T^{RF}$	TX RF weight matrix	$L_T \times L_T^{RF}$
$\mathbf{W}_R^{RF}$	RX RF weight matrix	$L_R \times L_R^{RF}$
$\mathbf{W}_{T,n}^{BB}$	TX BB weight matrix for n^{th} subcarrier	$L_T^{RF} \times U$
$\mathbf{w}_T^{RF}$	TX RF weight vector	$L_T \times 1$
$\mathbf{w}_R^{RF}$	RX RF weight vector	$L_R \times 1$

In the ABF JCAS case, in turn, the corresponding TX signal reads

$$\tilde{\mathbf{x}}_n^{ABF} = \mathbf{w}_T^{RF} x_n, \tag{5}$$

where $\mathbf{w}_T^{RF} \in \mathbb{C}^{L_T \times 1}$ stands for the TX RF weights applied for the single TX stream or TX sample x_n.

For readers' convenience, the main system model variables are summarized in Table I. We next proceed with establishing the radar received signal models and the applicable gain pattern expressions that form the basis for the beamforming optimization in Sections III and IV.

C. HBF JCAS: Radar Received Signal

From the sensing perspective, the transmitted beamformed signal propagates over-the-air and interacts with multiple targets, producing reflections that will be observed by the radar RX. In this work, we model the frequency-domain mm-wave channel based on well-established multipath models [17]. We assume K_t point targets with directions $\boldsymbol{\theta}_t = [\theta_{t,1}, \ldots, \theta_{t,K_t}]^T$. We note that, obviously, these angles are unknown by default to the JCAS system and correspond to the actual physical directions of the targets. The target reflections are modeled by the frequency-domain channel matrix $\mathbf{H}_{t,n} = \mathrm{diag}(h_{t,n,1}, \ldots, h_{t,n,K_t}) \in \mathbb{C}^{K_t \times K_t}$ where $\mathrm{diag}(\cdot)$ stands for the diagonal matrix with the argument entries $h_{t,n,k}$ on the diagonal. For the kth target reflection with $k = 1, \ldots, K_t$ and the nth subcarrier, the target channel reads

$$h_{t,n,k} = b_{t,n,k} e^{-j2\pi n \Delta f \tau_{t,k}} \text{ with}$$

$$b_{t,n,k} = \sqrt{\frac{\lambda_n^2 \sigma_{t,k}}{(4\pi)^3 d_{t,k}^4}}, \tag{6}$$

where $\tau_{t,k}$, $\sigma_{t,k}$, $d_{t,k}$ and $b_{t,n,k}$ denote the two-way propagation delay, the radar cross-section, the distance and the attenuation factor of the kth target based on the well-known *radar range equation* [31]. The variables λ_n and Δf refer to the wavelength of the nth subcarrier and the OFDM waveform subcarrier spacing, respectively.

Considering the monostatic radar operation and that the targets are in the far field, we can assume the angle-of-departure (AoD) and the angle-of-arrival (AoA) for each target to be approximately the same, $\theta_{t,k}$. The distance of each reflection can, in turn, be approximated as $d_{t,k} \approx \frac{\tau_{t,k} c_0}{2}$ where c_0 is the speed of light. Additionally, for an ideal TX ULA with L_T antennas with a separation of d_{ant} between neighboring antenna elements, the TX array steering vector can be expressed as

$$\mathbf{a}_{T,n}(\theta_{t,k}) = \left[1, e^{j\Phi_n(\theta_{t,k})}, \ldots, e^{j(L_T-1)\Phi_n(\theta_{t,k})}\right]^T, \quad (7)$$

where $\Phi_n(\theta_{t,k}) = 2\pi\frac{d_{ant}}{\lambda_n}\sin(\theta_{t,k})$ is the electrical AoD for the kth reflection. The RX array steering vector and the electrical AoA are obtained similarly. Then, the TX and RX steering matrices at the target directions $\boldsymbol{\theta}_t$ can be defined as $\mathbf{A}_{T,n}(\boldsymbol{\theta}_t) = [\mathbf{a}_{T,n}(\theta_{t,1}), \ldots, \mathbf{a}_{T,n}(\theta_{t,K_t})] \in \mathbb{C}^{L_T \times K_t}$ and $\mathbf{A}_{R,n}(\boldsymbol{\theta}_t) = [\mathbf{a}_{R,n}(\theta_{t,1}), \ldots, \mathbf{a}_{R,n}(\theta_{t,K_t})] \in \mathbb{C}^{L_R \times K_t}$, respectively.

Furthermore, the TX–RX coupling is represented by the SI channel matrix $\mathbf{H}_{SI,n} \in \mathbb{C}^{L_R \times L_T}$, with the entries $\{\mathbf{H}_{SI,n}\}_{l_R,l_T}$, $l_R = 1, \ldots, L_R$ and $l_T = 1, \ldots, L_T$, modeling the coupling channels between the l_T^{th} TX and the l_R^{th} RX antenna units. More details about the physical SI channel modelling are given in Section V. Therefore, the received spatial frequency-domain signal at the RX antenna elements can be expressed as

$$\tilde{\mathbf{y}}_n^{HBF} = \underbrace{\left(\mathbf{A}_{R,n}(\boldsymbol{\theta}_t)\mathbf{H}_{t,n}(\mathbf{A}_{T,n}(\boldsymbol{\theta}_t))^H + \mathbf{H}_{SI,n}\right)}_{\mathbf{H}_{r,n}}\tilde{\mathbf{x}}_n^{HBF} + \tilde{\mathbf{v}}_n, \quad (8)$$

where the noise vector $\tilde{\mathbf{v}}_n \in \mathbb{C}^{L_R \times 1}$ is assumed to be additive, white and Gaussian. In above, the effective multiantenna radar channel is represented by the channel matrix $\mathbf{H}_{r,n} \in \mathbb{C}^{L_R \times L_T}$ which incorporates both the actual target reflections and the SI leakage between the TX and RX antennas.

Finally, the spatial signal at the RX antenna elements is processed with the RX RF beamformer. This yields a frequency-domain beamformed received signal model of the form

$$\mathbf{y}_n^{HBF} = (\mathbf{W}_R^{RF})^H \tilde{\mathbf{y}}_n^{HBF} = (\mathbf{W}_R^{RF})^H \mathbf{H}_{r,n} \mathbf{W}_T^{RF} \mathbf{W}_{T,n}^{BB} \mathbf{x}_n + \mathbf{v}_n, \quad (9)$$

where $\mathbf{W}_R^{RF} \in \mathbb{C}^{L_R \times L_R^{RF}}$ refers to the radar RX RF weights and $\mathbf{v}_n = (\mathbf{W}_R^{RF})^H \tilde{\mathbf{v}}_n \in \mathbb{C}^{L_R^{RF} \times 1}$ denotes the beamformed noise vector. The beamformed spatial observed signal in (9) feeds then the actual radar processing algorithms. It is important to highlight that the expressions in (6) and (9) describe the radar point target channel and the radar received signal, respectively. The channels of the involved communication links can, in turn, be described with standard mm-wave scattering models as described for example in [17].

D. HBF JCAS: Gain Patterns

We next address and formulate the effective gain patterns for the considered HBF JCAS system. Considering the high carrier frequency and the subsequent wavelength being in the order

of millimeters, we assume far-field operation as the distances of the radar targets satisfy the conditions $d_{t,k} \gg \frac{(L_T d_{ant})^2}{\lambda_n}$ and $d_{t,k} \gg \frac{(L_R d_{ant})^2}{\lambda_n}$. Now, based on (4) and (8), the effective TX gain pattern for the uth stream can then be described as

$$G_{T,u,n}(\theta) = |(\mathbf{a}_{T,n}(\theta))^H \mathbf{W}_T^{RF} \mathbf{w}_{T,u,n}^{BB}|^2. \quad (10)$$

In the beamforming optimization, described in Section III, the BB weights of a particular user u can be designed to guarantee a minimum gain of $G_{T,u,n}(\theta_{c,u}) > \mu_u$ at the corresponding user direction $\theta_{c,u}$, with the value of μ_u being imposed by the communication performance requirements. At the same time, the BB weights can be used to minimize the interuser interference (IUI) by suppressing the effective TX response at the other users' directions, as $G_{T,u,n}(\theta_{c,u'}) \approx 0$ with $u' \neq u$.

Similarly, based on the expressions in (8) and (9), we express the RX gain pattern for the lth RX RF chain as

$$G_{R,l,n}^{RF}(\theta) = |(\mathbf{w}_{R,l}^{RF})^H \mathbf{a}_{R,l,n}(\theta)|^2, \quad (11)$$

where $\mathbf{w}_{R,l}^{RF} \in \mathbb{C}^{(L_R/L_R^{RF}) \times 1}$ and $\mathbf{a}_{R,l,n}(\theta) \in \mathbb{C}^{(L_R/L_R^{RF}) \times 1}$ with $l = 1, \ldots, L_R^{RF}$ denote the RF weights and the RX steering vector for the lth RX RF chain, respectively. Based on the subarray architecture shown in Fig. 1 and assuming that the antenna elements are equally distributed among all the RF chains, the RX RF weight matrix reads

$$\mathbf{W}_R^{RF} = \begin{bmatrix} \mathbf{w}_{R,1}^{RF} & \mathbf{0} & \cdots & \mathbf{0} \\ \mathbf{0} & \mathbf{w}_{R,2}^{RF} & \mathbf{0} & \vdots \\ \vdots & \mathbf{0} & \ddots & \mathbf{0} \\ \mathbf{0} & \cdots & \mathbf{0} & \mathbf{w}_{R,L_R^{RF}}^{RF} \end{bmatrix}, \quad (12)$$

where $\mathbf{0}$ denotes the zero vector. Additionally, the TX RF weights $\mathbf{W}_T^{RF}$ are distributed conceptually similarly to account for the considered subarray configuration in the TX side.

E. ABF JCAS: Radar Received Signal and Gain Patterns

We next present the corresponding radar received signal model and gain pattern expressions for the analog beam-forming JCAS architecture. To this end, assuming the TX spatial signal model in (5), the beamformed frequency-domain received signal at the sensing receiver can be expressed as

$$y_n^{ABF} = (\mathbf{w}_R^{RF})^H \underbrace{(\mathbf{H}_{r,n}\tilde{\mathbf{x}}_n^{ABF} + \tilde{\mathbf{v}}_n)}_{\tilde{\mathbf{y}}_n^{ABF}} = (\mathbf{w}_R^{RF})^H \mathbf{H}_{r,n} \mathbf{w}_T^{RF} x_n + v_n, \quad (13)$$

where $\mathbf{w}_T^{RF} \in \mathbb{C}^{L_T \times 1}$ and $\mathbf{w}_R^{RF} \in \mathbb{C}^{L_R \times 1}$ are the TX and RX RF beamforming weights, $v_n = (\mathbf{w}_R^{RF})^H \tilde{\mathbf{v}}_n \in \mathbb{C}$ is the beamformed noise sample and $\mathbf{H}_{r,n}$ is the effective radar channel matrix defined along (8). Similar to (10) and (11), the TX and RX gain patterns for the analog array JCAS architecture can now be expressed as

$$G_{T,n}^{RF}(\theta) = |(\mathbf{a}_{T,n}(\theta))^H \mathbf{w}_T^{RF}|^2,$$
$$G_{R,n}^{RF}(\theta) = |(\mathbf{w}_R^{RF})^H \mathbf{a}_{R,n}(\theta)|^2. \quad (14)$$

Furthermore, we define and adopt the so-called *combined radar pattern* (CRP), which refers to the total equivalent gain

pattern for the radar system [37]. In the ABF JCAS context, where TX and RX beam-patterns differ from each other, the CRP allows the evaluation of the overall radar performance. The CRP can be expressed by the multiplication of both the TX and RX gain patterns as

$$G_{\text{CRP},n}^{\text{RF}}(\theta) = G_{\text{T},n}^{\text{RF}}(\theta)G_{\text{R},n}^{\text{RF}}(\theta). \tag{15}$$

This CRP concept will be utilized along the ABF JCAS beamforming optimization, as discussed in greater details in Section IV-B.

III. BEAMFORMER DESIGN AND OPTIMIZATION: HYBRID MU-MIMO JCAS SYSTEM

In this section, we address the beamformer design and optimization challenge for the HBF JCAS systems. We leverage the so-called null-space projection (NSP) approach [38] for mitigating the SI and IUI phenomena, and construct solvable optimization problems to maximize the beamformed power of the sensing beam while controlling that of the communications beams according to the given communications constraints. As noted already in Section II, it is assumed that the JCAS transmitter has communication channel state information (CSI) only in the form of dominant path angles of the intended communication receivers. Further beamforming and equalization phases can be applied at the receiving terminal side, taking into account and correcting for the possible small-scale channel effects. The communication receiver side methods are, however, out of the scope of this article.

A. Null-Space Projection for SI and IUI Suppression

Building on the signal model in (9), the effective SI channel between the TX streams and the sensing RX RF chains can be first expressed as

$$\mathbf{C}_{\text{SI},n} = (\mathbf{W}_{\text{R}}^{\text{RF}})^H \mathbf{H}_{\text{SI},n} \mathbf{W}_{\text{T}}^{\text{RF}} \mathbf{W}_{\text{T},n}^{\text{BB}}, \tag{16}$$

with $\mathbf{C}_{\text{SI},n} \in \mathbb{C}^{L_{\text{R}}^{\text{RF}} \times U}$. Specifically, the elements $\{\mathbf{C}_{\text{SI},n}\}_{l,u}$ with $l = 1, \dots, L_{\text{R}}^{\text{RF}}$ and $u = 1, \dots, U$ represent the effective SI channel between the uth user stream and the lth RX RF chain at subcarrier n. To suppress the SI in the lth receive chain, the corresponding RX beamformer weights $\mathbf{w}_{\text{R},l}^{\text{RF}}$ should satisfy the following condition:

$$\mathbf{c}_{\text{SI},n,l} = (\mathbf{w}_{\text{R},l}^{\text{RF}})^H \mathbf{H}_{\text{SI},n} \mathbf{W}_{\text{T}}^{\text{RF}} \mathbf{W}_{\text{T},n}^{\text{BB}} = \mathbf{0}^T, \tag{17}$$

where $\mathbf{c}_{\text{SI},n,l} \in \mathbb{C}^{1 \times U}$ represents the lth row of the matrix in (16). While the above condition is expressed for a particular subcarrier n, it can be extended to cover $\mathcal{N}_{\text{freq}}$ subcarriers over the whole transmission bandwidth and subsequently to suppress wideband SI signal. This is expressed as

$$(\mathbf{w}_{\text{R},l}^{\text{RF}})^H \underbrace{\left[\hat{\mathbf{H}}_{\text{SI},n_1} \mathbf{W}_{\text{T}}^{\text{RF}} \mathbf{W}_{\text{T},n_1}^{\text{BB}}, \dots, \hat{\mathbf{H}}_{\text{SI},n_{\mathcal{N}_{\text{freq}}}} \mathbf{W}_{\text{T}}^{\text{RF}} \mathbf{W}_{\text{T},n_{\mathcal{N}_{\text{freq}}}}^{\text{BB}} \right]}_{=\mathbf{B}_l}$$
$$= (\mathbf{w}_{\text{R},l}^{\text{RF}})^H \mathbf{B}_l = \mathbf{0}^T, \tag{18}$$

where $n_1, \dots, n_{\mathcal{N}_{\text{freq}}}$ denote the subcarrier indices for which the NSP method is considered. Furthermore, as the multi-antenna SI channel is not known by default, the corresponding SI channel estimate, denoted by $\hat{\mathbf{H}}_{\text{SI},n} \in \mathbb{C}^{L_R \times L_T}$, is utilized

in the above expression. The impacts of imperfect SI channel estimation accuracy are addressed along the numerical results. We note that the NSP method used to suppress the interference may slightly impact the beamforming performance. Therefore, we investigate the potential performance degradation in Section V-C.

Similar to [39], the NSP matrix can be deduced from (18) based on the Moore–Penrose pseudoinverse approach $(\mathbf{B}_l(\mathbf{B}_l)^\dagger \mathbf{B}_l = \mathbf{B}_l)$, expressed as

$$\mathbf{N}_{\text{SI},l} = (\mathbf{I} - \mathbf{B}_l(\mathbf{B}_l)^\dagger). \tag{19}$$

Based on (19), we can thus reformulate the wideband NSP condition in (18) as

$$(\tilde{\mathbf{w}}_{\text{R},l}^{\text{RF}})^H \mathbf{N}_{\text{SI},l} \mathbf{B}_l = \mathbf{0}^T, \tag{20}$$

where $\mathbf{w}_{\text{R},l}^{\text{RF}} = (\mathbf{N}_{\text{SI},l})^H \tilde{\mathbf{w}}_{\text{R},l}^{\text{RF}}$. In the actual beamforming design addressed in the next subsection, the auxiliary vector $\tilde{\mathbf{w}}_{\text{R},l}^{\text{RF}} \in \mathbb{C}^{(L_{\text{R}}/L_{\text{R}}^{\text{RF}}) \times 1}$ will be optimized. Finally, we define and quantify the average achieved SI suppression among the overall transmission bandwidth with a total of N subcarriers as

$$\bar{c}_{\text{SI},l,u} = \frac{1}{N} \sum_{n=0}^{N-1} |c_{\text{SI},n,l,u}|^2, \tag{21}$$

where $c_{\text{SI},n,l,u} = \{\mathbf{C}_{\text{SI},n}\}_{l,u}$.

A similar NSP approach can be employed to also suppress the IUI in the hybrid MU-MIMO JCAS system. To this end, the TX BB weights of the uth user can be used to minimize the IUI by suppressing the effective TX response at the other users' directions, i.e., $G_{\text{T},u,n}(\theta_{\text{c},u'}) \approx 0$ with $u' \neq u$. Based on (10), the corresponding NSP condition for the IUI can now be expressed as

$$\underbrace{\left[(\mathbf{a}_{\text{T},n}(\theta_{\text{c},1}))^H \mathbf{W}_{\text{T}}^{\text{RF}}, \dots, (\mathbf{a}_{\text{T},n}(\theta_{\text{c},U'}))^H \mathbf{W}_{\text{T}}^{\text{RF}} \right]}_{\mathbf{D}_{u,n}} \mathbf{w}_{\text{T},u,n}^{\text{BB}} = \mathbf{0}. \tag{22}$$

Finally, the TX BB weights are defined with the help of the corresponding NSP matrices $\mathbf{N}_{\text{IUI},u,n} = (\mathbf{I} - (\mathbf{D}_{u,n})^\dagger \mathbf{D}_{u,n})$ as

$$\mathbf{W}_{\text{T},n}^{\text{BB}} = [\mathbf{N}_{\text{IUI},1,n} \tilde{\mathbf{w}}_{\text{T},1,n}^{\text{BB}}, \dots, \mathbf{N}_{\text{IUI},U,n} \tilde{\mathbf{w}}_{\text{T},U,n}^{\text{BB}}], \tag{23}$$

where $\tilde{\mathbf{w}}_{\text{T},u,n}^{\text{BB}} \in \mathbb{C}^{L_{\text{T}}^{\text{RF}} \times 1}$ while $\mathbf{w}_{\text{T},u,n}^{\text{BB}} = \mathbf{N}_{\text{IUI},u,n} \tilde{\mathbf{w}}_{\text{T},u,n}^{\text{BB}}$ denotes the auxiliary weight vector used along the beamforming optimization.

B. Beamforming Optimization

The proposed hybrid MU-MIMO JCAS beamforming design jointly optimizes the TX RF and BB weights to maximize the TX power at any given radar direction θ_{r}. This beamformed power can be expressed as

$$P_{\text{T,r},n} = \mathbb{E}\{|(\mathbf{a}_{\text{T},n}(\theta_{\text{r}}))^H \mathbf{W}_{\text{T}}^{\text{RF}} \mathbf{W}_{\text{T},n}^{\text{BB}} \mathbf{x}_n|^2\}$$
$$= \sum_{u=1}^{U} \mathbb{E}\{|(\mathbf{a}_{\text{T},n}(\theta_{\text{r}}))^H \mathbf{W}_{\text{T}}^{\text{RF}} \mathbf{w}_{\text{T},n,u}^{\text{BB}} x_{u,n}|^2\}$$
$$= \sum_{u=1}^{U} G_{\text{T},u,n}(\theta_{\text{r}}) P_{u,n}, \tag{24}$$

where $P_{u,n} = \mathbb{E}\{|x_{u,n}|^2\}$ and $G_{\mathrm{T},u,n}(\theta_{\mathrm{r}})$ denote the uth user stream's TX power and the effective TX gain at the radar direction for the nth subcarrier defined in (10), respectively.

For notational simplicity, the beamformer optimization is next formulated for the subcarrier located at the center of the channel — denoted with n_{c}. Based on (24) and (10), the TX BB and RF weights, $\mathbf{W}_{\mathrm{T},n_{\mathrm{c}}}^{\mathrm{BB}}$ and $\mathbf{W}_{\mathrm{T}}^{\mathrm{RF}}$, are obtained by defining and solving the following optimization problem:

$$\max_{\tilde{\mathbf{W}}_{\mathrm{T},n_{\mathrm{c}}}^{\mathrm{BB}},\mathbf{W}_{\mathrm{T}}^{\mathrm{RF}}} \sum_{u=1}^{U} G_{\mathrm{T},u,n_{\mathrm{c}}}(\theta_{\mathrm{r}}) \tag{25a}$$

$$\text{s.t. } \left\| \mathbf{W}_{\mathrm{T}}^{\mathrm{RF}} \mathbf{w}_{\mathrm{T},u,n_{\mathrm{c}}}^{\mathrm{BB}} \right\| = 1, \ \forall u, \tag{25b}$$

$$G_{\mathrm{T},u,n_{\mathrm{c}}}(\theta_{\mathrm{c},u}) \geq \mu_u, \ \forall u, \tag{25c}$$

$$\mathbf{W}_{\mathrm{T},n_{\mathrm{c}}}^{\mathrm{BB}} = [\mathbf{N}_{\mathrm{IUI},1,n_{\mathrm{c}}} \tilde{\mathbf{w}}_{\mathrm{T},1,n_{\mathrm{c}}}^{\mathrm{BB}}, \ldots, \mathbf{N}_{\mathrm{IUI},U,n_{\mathrm{c}}} \tilde{\mathbf{w}}_{\mathrm{T},U,n_{\mathrm{c}}}^{\mathrm{BB}}]. \tag{25d}$$

The effective TX powers are normalized by (25b). In addition, the minimum effective TX gain for the uth user at the specific user direction $\theta_{\mathrm{c},u}$ is constrained in (25c), where μ_u is the required minimum gain imposed by the communication system and the corresponding performance requirements. The minimum required gain is directly related with the channel of each user, therefore, different users may require different value for μ_u. Therefore, this parameter can be set independently for each user in (25c). Finally, in (25d), the null-space projection structure in (23) is imposed such that optimization is performed over the auxiliary BB weight matrix $\tilde{\mathbf{W}}_{\mathrm{T},n_{\mathrm{c}}}^{\mathrm{BB}} = [\tilde{\mathbf{w}}_{\mathrm{T},1,n_{\mathrm{c}}}^{\mathrm{BB}}, \ldots, \tilde{\mathbf{w}}_{\mathrm{T},U,n_{\mathrm{c}}}^{\mathrm{BB}}] \in \mathbb{C}^{L_{\mathrm{T}}^{\mathrm{RF}} \times U}$ to effectively suppress the IUI. We note that the NSP constraint in (25d) may be removed or omitted from the optimization problem in scenarios where the IUI is not critical; in such cases, it is expected that higher radar gains can be achieved. In our numerical experiments, the optimization problem is solved via the `fmincon` function of the MATLAB optimization toolbox.

At the RX side, the goal is to maximize the RX beamforming gain at the radar direction $G_{\mathrm{R},l,n_{\mathrm{c}}}^{\mathrm{RF}}(\theta_{\mathrm{r}})$ for each RF chain, while the SI is effectively suppressed through the NSP approach described in Section III-A. Thus, the RF weights of the lth RX RF chain are obtained by solving the following optimization problem:

$$\max_{\tilde{\mathbf{w}}_{\mathrm{R},l}^{\mathrm{RF}}} |(\tilde{\mathbf{w}}_{\mathrm{R},l}^{\mathrm{RF}})^H \mathbf{N}_{\mathrm{SI},l} \mathbf{a}_{\mathrm{R},l,n_{\mathrm{c}}}(\theta_{\mathrm{r}})|^2 \tag{26a}$$

$$\text{s.t. } \left\| \mathbf{w}_{\mathrm{R},l}^{\mathrm{RF}} \right\| = 1, \tag{26b}$$

where $\mathbf{w}_{\mathrm{R},l}^{\mathrm{RF}} = (\mathbf{N}_{\mathrm{SI},l})^H \tilde{\mathbf{w}}_{\mathrm{R},l}^{\mathrm{RF}}$. This essentially leads to a spatial matched filter-like approach that is optimized through a proper phase alignment. Furthermore, from the NSP matrix definition in (19), we can observe that $\mathbf{N}_{\mathrm{SI},l}$ is a Hermitian and idempotent matrix ($\mathbf{N}_{\mathrm{SI},l} = (\mathbf{N}_{\mathrm{SI},l})^H = \mathbf{N}_{\mathrm{SI},l}\mathbf{N}_{\mathrm{SI},l}$). Thus, we can derive the optimal RX weights as

$$\mathbf{w}_{\mathrm{R},l}^{\mathrm{RF}} = \frac{(\mathbf{N}_{\mathrm{SI},l})^H \tilde{\mathbf{w}}_{\mathrm{R},l}^{\mathrm{RF}}}{\left\| (\mathbf{N}_{\mathrm{SI},l})^H \tilde{\mathbf{w}}_{\mathrm{R},l}^{\mathrm{RF}} \right\|} = \frac{(\mathbf{N}_{\mathrm{SI},l})^H \mathbf{N}_{\mathrm{SI},l} \mathbf{a}_{\mathrm{R},l,n_{\mathrm{c}}}(\theta_{\mathrm{r}})}{\left\| (\mathbf{N}_{\mathrm{SI},l})^H \mathbf{N}_{\mathrm{SI},l} \mathbf{a}_{\mathrm{R},l,n_{\mathrm{c}}}(\theta_{\mathrm{r}}) \right\|}$$

$$= \frac{\mathbf{N}_{\mathrm{SI},l} \mathbf{a}_{\mathrm{R},l,n_{\mathrm{c}}}(\theta_{\mathrm{r}})}{\left\| \mathbf{N}_{\mathrm{SI},l} \mathbf{a}_{\mathrm{R},l,n_{\mathrm{c}}}(\theta_{\mathrm{r}}) \right\|}. \tag{27}$$

IV. BEAMFORMER DESIGN AND OPTIMIZATION: ANALOG ARRAY JCAS SYSTEM

We next propose and formulate beamforming design and optimization methods for the analog array JCAS architecture such that the selected beamformed communications requirements are met, while maximizing the ability to simultaneously sense targets in another direction. Both closed-form and numerical optimization based methods will be provided, while the main differences compared to the previous hybrid MU-MIMO system model are that only RF beamformers and one spatial stream per subcarrier are considered. Again, similar to Section III, it is assumed that the only CSI available to the JCAS transmitter contains the dominant path angles of the intended communication receivers.

A. Closed-Form Solution

Building on the ABF JCAS signal and system models in Section II, we provide a closed-form (CF) beamforming design procedure to define the TX and RX beamforming weights, $\mathbf{w}_{\mathrm{T}}^{\mathrm{RF}}$ and $\mathbf{w}_{\mathrm{R}}^{\mathrm{RF}}$, respectively. At the TX side, we first generate separate weights for the corresponding communication and sensing beams. This can be achieved by choosing the TX RF weights to maximize the TX beamforming gain $G_{\mathrm{T},n_{\mathrm{c}}}^{\mathrm{RF}}(\theta)$ at the given desired direction θ, expressed formally as

$$\max_{\mathbf{w}_{\mathrm{T}}^{\mathrm{RF}}(\theta)} |(\mathbf{a}_{\mathrm{T},n_{\mathrm{c}}}(\theta))^H \mathbf{w}_{\mathrm{T}}^{\mathrm{RF}}(\theta)|^2 \tag{28a}$$

$$\text{s.t. } \left\| \mathbf{w}_{\mathrm{T}}^{\mathrm{RF}}(\theta) \right\| = 1. \tag{28b}$$

This yields the following normalized weights

$$\mathbf{w}_{\mathrm{T}}^{\mathrm{RF}}(\theta) = \frac{\mathbf{a}_{\mathrm{T},n_{\mathrm{c}}}(\theta)}{\left\| \mathbf{a}_{\mathrm{T},n_{\mathrm{c}}}(\theta) \right\|}. \tag{29}$$

Then, similar to [24], [27], [40], the communication and sensing weights are combined coherently. Considering the U communication beams and a single sensing beam, all coexisting simultaneously, the combined TX weights can be expressed as

$$\mathbf{w}_{\mathrm{T}}^{\mathrm{RF}} = \sqrt{\rho_{\mathrm{r}}} \mathbf{w}_{\mathrm{T}}^{\mathrm{RF}}(\theta_{\mathrm{r}}) + \sum_{u=1}^{U} \sqrt{\rho_{\mathrm{c},u}} \mathbf{w}_{\mathrm{T}}^{\mathrm{RF}}(\theta_{\mathrm{c},u}), \tag{30}$$

where $\mathbf{w}_{\mathrm{T}}^{\mathrm{RF}}(\theta_{\mathrm{r}})$ and $\mathbf{w}_{\mathrm{T}}^{\mathrm{RF}}(\theta_{\mathrm{c},u})$ are the individually optimized TX RF weights for sensing and communications, respectively. The ρ-parameters control the energy distribution between the beamforming weights and subsequently the overall communication and radar performance. In particular, ρ_{r} and $\rho_{\mathrm{c},u}$, with $\rho_{\mathrm{r}} + \sum_{u=1}^{U} \rho_{\mathrm{c},u} = 1$, control the energy of the sensing and the uth communication beams, respectively. The obtained TX weights $\mathbf{w}_{\mathrm{T}}^{\mathrm{RF}}$ are further normalized as $\left\| \mathbf{w}_{\mathrm{T}}^{\mathrm{RF}} \right\| = 1$.

We then formulate a generalized optimization problem for designing the RX beamforming weights similar to (26), expressed as

$$\max_{\tilde{\mathbf{w}}_{\mathrm{R}}^{\mathrm{RF}}} |(\tilde{\mathbf{w}}_{\mathrm{R}}^{\mathrm{RF}})^H \mathbf{N}_{\mathrm{RF}} \mathbf{a}_{\mathrm{R},n_{\mathrm{c}}}(\theta_{\mathrm{r}})|^2 \tag{31a}$$

$$\text{s.t. } \left\| \mathbf{w}_{\mathrm{R}}^{\mathrm{RF}} \right\| = 1, \tag{31b}$$

where $\mathbf{w}_{\mathrm{R}}^{\mathrm{RF}} = (\mathbf{N}_{\mathrm{RF}})^H \tilde{\mathbf{w}}_{\mathrm{R}}^{\mathrm{RF}}$ and $\mathbf{N}_{\mathrm{RF}} = (\mathbf{I} - \mathbf{F}\mathbf{F}^\dagger)$. Furthermore, compared to (26), we extend the considered NSP

TABLE II

DIFFERENT CONFIGURATIONS FOR THE RX BEAMFORMER IN ABF JCAS SYSTEMS, WHERE $\mathcal{N}_{\text{FREQ}}$ AND $\mathcal{N}_{\text{ANG}}$ DENOTE THE NUMBERS OF FREQUENCY BINS AND ANGULAR DIRECTIONS FOR WHICH THE SI AND COMMUNICATION BEAM IMPACTS ARE NULLED, RESPECTIVELY

	CF-A	CF-B	CF-C
SI suppression	–	$\mathcal{N}_{\text{freq}}$	$\mathcal{N}_{\text{freq}}$
Communication beam suppression	–	–	$\mathcal{N}_{\text{ang}}$

approach to simultaneously cancel the impact of the communication beam direction at the RX pattern. Based on (18) and (22), we thus generalize the NSP matrix incorporating $\mathcal{N}_{\text{freq}}$ frequency nulls to suppress the SI and $\mathcal{N}_{\text{ang}}$ angular nulls to cancel the reflections due to the communication beams, expressed formally as

$$\mathbf{F} = [\underbrace{\hat{\mathbf{H}}_{\text{SI},n_1}\mathbf{w}_{\text{T}}^{\text{RF}}, \ldots, \hat{\mathbf{H}}_{\text{SI},n_{\mathcal{N}_{\text{freq}}}}\mathbf{w}_{\text{T}}^{\text{RF}}}_{\mathcal{N}_{\text{freq}} \text{ frequency nulls}},$$
$$\underbrace{\mathbf{a}_{\text{R},n_{\text{c}}}(\theta_1), \ldots, \mathbf{a}_{\text{R},n_{\text{c}}}(\theta_{\mathcal{N}_{\text{ang}}})}_{\mathcal{N}_{\text{ang}} \text{ angular nulls}}]. \quad (32)$$

Finally, the RX RF weights for the analog array JCAS architecture are normalized as

$$\mathbf{w}_{\text{R}}^{\text{RF}} = \frac{\mathbf{N}_{\text{RF}}\mathbf{a}_{\text{R},n_{\text{c}}}(\theta_{\text{r}})}{\|\mathbf{N}_{\text{RF}}\mathbf{a}_{\text{R},n_{\text{c}}}(\theta_{\text{r}})\|}. \quad (33)$$

For presentation clarity, we summarize the different RX beamforming configurations in Table II. The basic reference scheme from [24], denoted by CF-A, does not pursue SI nor communication beam suppression. In this case, the RX weights are just optimized to provide a radar beam by $\mathbf{N}_{\text{RF}} = \mathbf{I}$. The second configuration, denoted by CF-B, incorporates $\mathcal{N}_{\text{freq}}$ frequency nulls in the NSP matrix definition to effectively suppress the SI signal. Finally, the third configuration CF-C is the most general and sophisticated, including $\mathcal{N}_{\text{freq}}$ frequency nulls and $\mathcal{N}_{\text{ang}}$ angular nulls to suppress the SI and the communication beam interference, respectively. We note that along the numerical results in Section V, the performance of the proposed beamforming methods are compared with the CF-A scheme from [24], showing substantial improvements from both beamforming and SI cancellation perspectives.

B. CPSL-Based Optimization Solution

The beamforming solution described in Section IV-A addresses both the SI leakage as well as the communication beam interference in the ABF JCAS context. However, to further improve the capability to suppress the communication beam interference in terms of, e.g., clutter from the environment, we next pursue a numerical optimization based beamformer design approach. Specifically, we formulate an optimization problem to design the RX RF beamforming weights that minimize the negative effects of the TX communication beams, by optimizing the combined peak sidelobe level (CPSL) of the CRP, while also efficiently suppressing the harmful SI leakage. To this end, a constrained least-squares
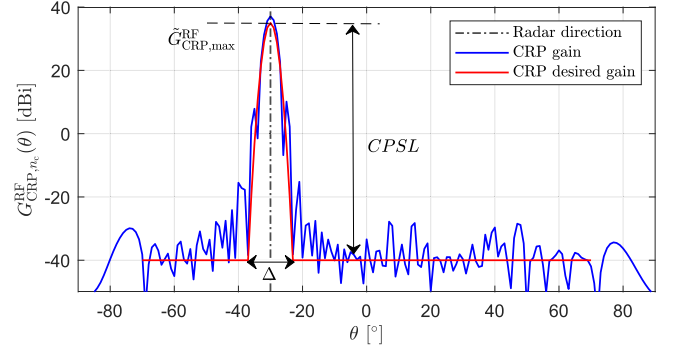
Fig. 2. Illustration of a CRP with directional radar beam at $\theta_{\text{r}} = -30°$. The proposed RX RF beamforming design seeks to provide a CRP that approximates well the desired gain pattern with $\tilde{G}_{\text{CRP,max}}^{\text{RF}}$, Δ and $CPSL$ denoting the maximum gain of the CRP at the radar direction, the mask's width around the radar direction and the desired CPSL of the CRP, respectively.

problem is formulated as

$$\min_{\tilde{\mathbf{w}}_{\text{R}}^{\text{RF}}} \frac{1}{S} \sum_{s=1}^{S} \eta_s \left| G_{\text{CRP},n_{\text{c}}}^{\text{RF}}(\theta_s) - \tilde{G}_{\text{CRP},n_{\text{c}}}^{\text{RF}}(\theta_s) \right|^2 \quad (34a)$$

$$\text{s.t.} \ \left\| \mathbf{w}_{\text{R}}^{\text{RF}} \right\| = 1, \quad (34b)$$

where $\mathbf{w}_{\text{R}}^{\text{RF}} = (\mathbf{N}_{\text{RF}})^H \tilde{\mathbf{w}}_{\text{R}}^{\text{RF}}$ and the NSP matrix $\mathbf{N}_{\text{RF}}$ implements $\mathcal{N}_{\text{freq}}$ frequency nulls as described in (32). The main goal of the optimization is to provide a CRP $G_{\text{CRP},n_{\text{c}}}^{\text{RF}}(\theta_s)$ that best approximates the desired ideal CRP $\tilde{G}_{\text{CRP},n_{\text{c}}}^{\text{RF}}(\theta_s)$ described in (35), in least-squares sense, at the defined directions θ_s with $s = 1, \ldots, S$. Additional weights η_s, $s = 1, \ldots, S$, are allowed in the optimization to control and emphasize the error at specific directions. We note that the above problem is convex and can be efficiently solved by numerical tools [41]. In our numerical results, the RF weights are obtained using the fmincon function of the optimization toolbox of MATLAB.

In general, the CRP needs to provide a single beam at the sensing direction while the CPSL is minimized at the rest of directions. The notion of an ideal CRP is subject to definition, particularly when it comes to the mainlobe shape and width, and the targeted sidelobe suppression level. However, in this work, we provide one concrete and implementation feasible example based on the piecewise parabolic function, expressed as

$$\tilde{G}_{\text{CRP},n_{\text{c}}}^{\text{RF}}(\theta_s) = \begin{cases} \frac{(\theta_s - \theta_{\text{r}})^2 CPSL}{\Delta^2/4} + \tilde{G}_{\text{CRP,max}}^{\text{RF}} & \text{if } |\theta_s - \theta_{\text{r}}| \leq \frac{\Delta}{2} \\ \tilde{G}_{\text{CRP,max}}^{\text{RF}} + CPSL & \text{if } |\theta_s - \theta_{\text{r}}| > \frac{\Delta}{2} \end{cases}$$
$$(35)$$

where $\tilde{G}_{\text{CRP,max}}^{\text{RF}}$, Δ and $CPSL$ denote the maximum gain of the CRP at the radar direction, the mask's width around the radar direction and the desired CPSL of the CRP, respectively. Figure 2 presents an illustrative example of the CPSL optimization approach showing the main design parameters.

V. NUMERICAL RESULTS

In this section, we numerically evaluate the proposed JCAS beamforming methods for both the hybrid MU-MIMO and

the analog array architectures. In these numerical evaluations, we consider a realistic linear patch array simulated with CST Studio Suite, including the coupling effects between TX and RX elements to accurately model and investigate the SI phenomenon and its suppression. In particular, a linear array of 64 elements is used, with $L_T = 32$ TX and $L_R = 32$ RX elements. The SI channel matrix is obtained from the S-parameters of the electromagnetic (EM) simulations describing the relation of the input and output voltage waves at each physical antenna port. The first 32 ports are assigned for the transmitter and the remaining 32 for the receiver. This is expressed mathematically as $\{\mathbf{H}_{\mathrm{SI},n}\}_{l_R,l_T} = S_{ij}$, where $i = l_T$ and $j = L_T + l_R$. The system's center frequency is assumed to be 28 GHz while a nominal channel bandwidth of 500 MHz is considered.

Finally, while the true SI channel characteristics $\mathbf{H}_{\mathrm{SI},n}$ are provided by the electromagnetic simulations, we model the non-ideal estimation process through additive SI channel estimation error $\tilde{\mathbf{H}}_{\mathrm{SI},n} \in \mathbb{C}^{L_R \times L_T}$, expressed formally as

$$\hat{\mathbf{H}}_{\mathrm{SI},n} = \mathbf{H}_{\mathrm{SI},n} + \tilde{\mathbf{H}}_{\mathrm{SI},n}. \tag{36}$$

In the numerical evaluations, we assume all the elements of $\tilde{\mathbf{H}}_{\mathrm{SI},n}$ to be independent complex Gaussian random variables, and the relative estimation error level is controlled by the parameter

$$\epsilon^2 = \frac{\mathbb{E}\{|\{\tilde{\mathbf{H}}_{\mathrm{SI},n}\}_{l_R,l_T}|^2\}}{\frac{1}{L_T L_R} \sum_{l_R=1}^{L_R} \sum_{l_T=1}^{L_T} |\{\mathbf{H}_{\mathrm{SI},n}\}_{l_R,l_T}|^2}, \tag{37}$$

for all l_R and l_T. Although the SI channel estimation as such is not directly within the scope of this paper, we identify possible alternatives to estimate the SI channel in practical implementations. The first alternative considers an additional observation receiver that measures the coupling channel between different TX and RX antenna ports. Another and perhaps more implementation feasible possibility is to measure the corresponding SI channel in a calibration phase. In addition, EM simulation data of the SI coupling channel can be also used for beamforming optimization. Regardless of the estimation strategy, in practice, the estimated SI channel $\hat{\mathbf{H}}_{\mathrm{SI},n}$ will be non-ideal, therefore, it is highly important to analyze the performance of the proposed methods accordingly.

A. Hybrid MU-MIMO JCAS Architecture

We first consider a hybrid MU-MIMO JCAS architecture when $L_T^{\mathrm{RF}} = 8$ and $L_R^{\mathrm{RF}} = 4$ RF chains are adopted at the TX and RX sides, respectively. Furthermore, we assume that $U = 2$ and that the JCAS system provides two communication beams for the two users located at $\theta_{\mathrm{c},1} = -30°$ and $\theta_{\mathrm{c},2} = 30°$, respectively, with the minimum TX gains of $\mu_1 = \mu_2 = 15$ dBi considered in the beamforming optimization in (25c). Additionally, the TX power at the assumed radar direction of $\theta_r = 10°$ is maximized by generating a separate beam for sensing the environment, as described in Section III-B.

The respective optimized beam-patterns are illustrated in Fig. 3. Specifically, Fig. 3(a) shows the effective TX patterns for each of the two transmitted streams. As it can be observed,
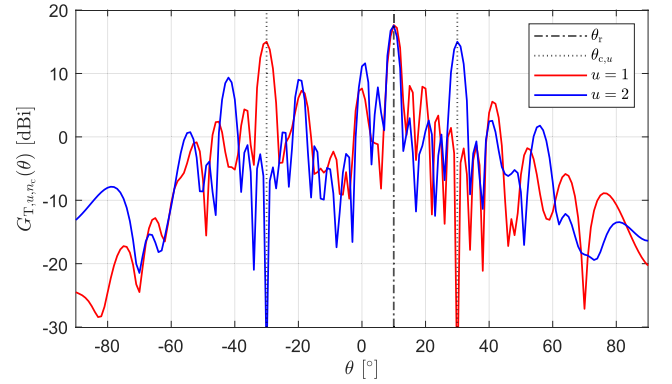
(a) Effective TX beam-patterns of the two streams
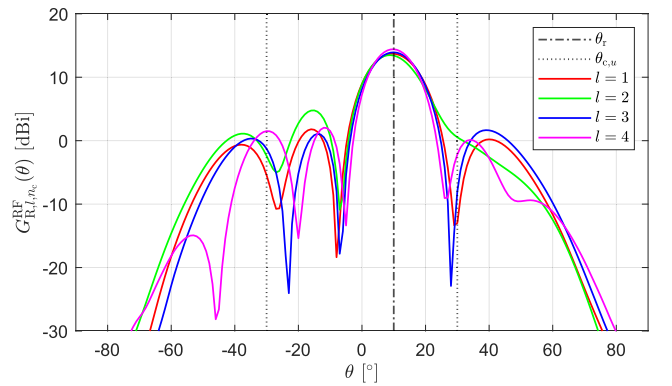
(b) RX beam-patterns of the four subarrays

Fig. 3. Illustration of the relevant beam-patterns in a hybrid MU-MIMO JCAS system with a radar beam at $\theta_r = 10°$ and $U = 2$ communication users located at $\theta_{\mathrm{c},1} = -30°$ and $\theta_{\mathrm{c},2} = 30°$, respectively. The rest of the system parameters are $L_T = L_R = 32$, $L_T^{\mathrm{RF}} = 8$, $L_R^{\mathrm{RF}} = 4$, $\mu_1 = \mu_2 = 15$ dBi, and $\mathcal{N}_{\mathrm{freq}} = 2$.

each effective pattern provides two beams, one for communication and another one for sensing, while the IUI is minimized by imposing a null at the other user's direction as explained in (25). For example, the $u = 1$ stream provides two beams at $\theta_{\mathrm{c},1} = -30°$ and $\theta_r = 10°$ while cancelling the $\theta_{\mathrm{c},2} = 30°$ direction. Fig. 3(b) shows the corresponding RX beam-patterns for the different RX RF chains (different subarrays). As it can be seen, each subarray connected to a particular RX RF chain generates a directive beam at the radar direction for observing the reflections. In addition, the RX weights are optimized to cancel the SI as will be explicitly illustrated in Section V-C, namely Fig. 6 therein.

Figure 4 illustrates and analyzes the effects of the minimum required TX gain imposed by the communication system into the achievable radar performance. In this case, we consider a similar scenario to Fig. 3 with $U = 2$ communication users with $\mu_1 = \mu_2$. Moreover, different hybrid architectures are investigated by varying the number of TX RF chains. Note that the specific case of $L_T^{\mathrm{RF}} = L_T = 32$ corresponds already to full digital TX beamforming. The figure shows the behavior of the optimized radar gain, expressed in (24), for different values of μ_u. As can be observed, varying the parameter μ_u provides a trade-off between the communication
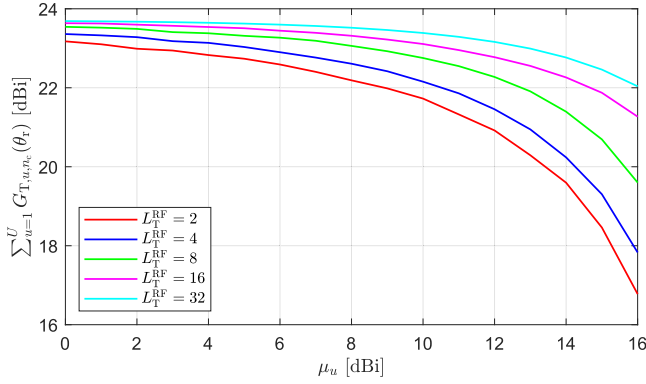
Fig. 4. Illustration of the achievable beamformed radar TX gain in hybrid MU-MIMO JCAS context for varying communication TX gain μ_u and different numbers of TX RF chains $L_{\mathrm{T}}^{\mathrm{RF}}$. In this analysis, we assume the following parameters of $U = 2$, $\theta_{\mathrm{r}} = 10°$, $\theta_{\mathrm{c},1} = -30°$, $\theta_{\mathrm{c},2} = 30°$, $\mu_1 = \mu_2 = \mu_u$ and $L_{\mathrm{T}} = 32$. The specific case of $L_{\mathrm{T}}^{\mathrm{RF}} = L_{\mathrm{T}} = 32$ corresponds to full digital TX beamforming.

and sensing performances. For relatively low values of μ_u, the JCAS system allows more flexibility for sensing, providing higher gains at the radar direction. In contrast, when higher gains are required for communications beams (high values of μ_u), the JCAS system will decrease the radar performance. In addition, we can see how the different parametrizations of the hybrid architecture impact the final sensing performance. In this regard, the configurations with more TX RF chains and subsequently more flexibility in the digital domain TX processing, show better beamforming performance.

B. Analog Array JCAS Architecture

Next, we study and illustrate the beam-patterns in the analog array based JCAS architecture. Specifically, we pursue the multibeam operation with $U = 2$ communication users located at $\theta_{\mathrm{c},1} = -40°$ and $\theta_{\mathrm{c},2} = 40°$, respectively, together with one simultaneous sensing beam at $\theta_{\mathrm{r}} = 10°$. The array sizes are as noted in the beginning of this section, namely $L_{\mathrm{T}} = L_{\mathrm{R}} = 32$ while $\mathcal{N}_{\mathrm{freq}} = 2$.

The obtained beam-patterns are illustrated in Fig. 5. Specifically, at the TX side, the weights of the three considered beams are first separately optimized based on (29) while then combined according to (30) wherein we further assume $\rho_{\mathrm{r}} = \rho_{\mathrm{c},1} = \rho_{\mathrm{c},2} = 1/3$. The obtained corresponding TX beam-pattern is illustrated in Fig. 5(a) showing well-behaving beams at the three indicated directions. At the RX side, in turn, the two closed-form solutions called CF-B and CF-C are first explored, and illustrated in Fig. 5(b). In the CF-B configuration, only SI suppression is pursued, in addition to providing coherent combining at the radar direction. In the more advanced CF-C configuration, in turn, additional angular nulls are considered in the RX side, as described in (32), in order to also suppress the possible negative effects of the communication beams on the overall sensing performance. In this case, two angular nulls ($\mathcal{N}_{\mathrm{ang}} = 2$) are deployed at the corresponding communication directions. As can be observed in Fig. 5(c), the CF-C configuration is able to suppress the contribution of the communication beams in the CRP.
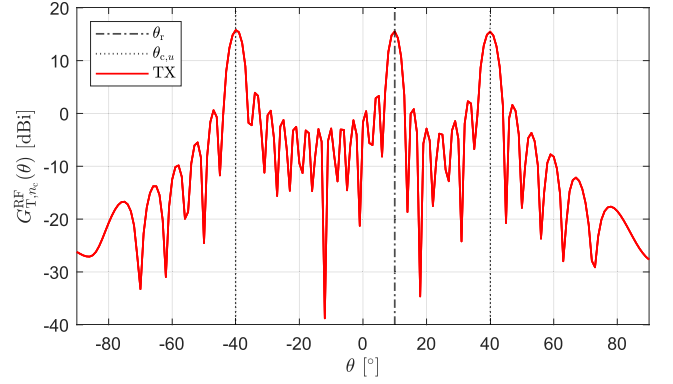
(a) TX beam-pattern [24]
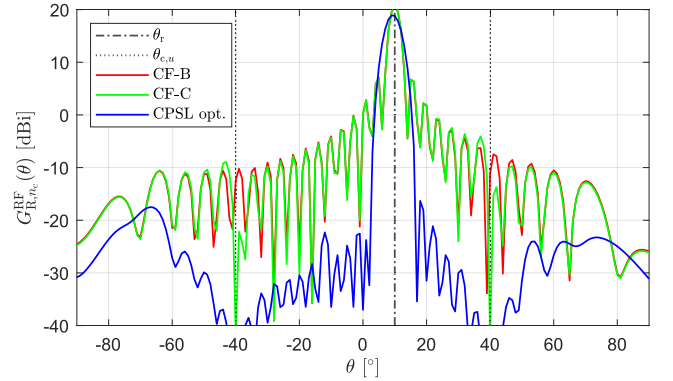
(b) RX beam-patterns
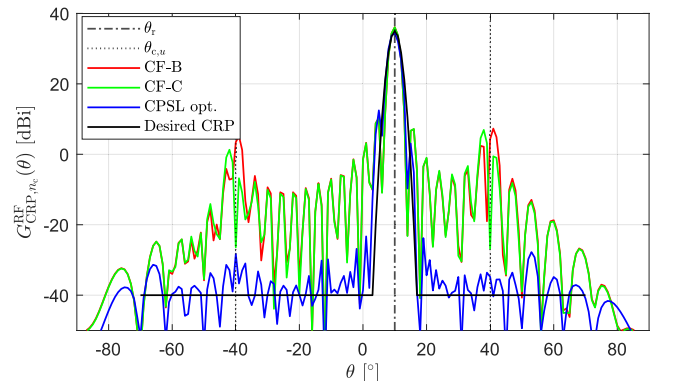
(c) Combined radar beam-patterns

Fig. 5. Illustration of the beam-patterns with analog array JCAS architecture, with a radar beam at $\theta_{\mathrm{r}} = 10°$ and $U = 2$ communication users located at $\theta_{\mathrm{c},1} = -40°$ and $\theta_{\mathrm{c},2} = 40°$, respectively. At the TX side, three beams are designed with the same relative energy share of $\rho_{\mathrm{r}} = \rho_{\mathrm{c},1} = \rho_{\mathrm{c},2} = 1/3$. In the CPSL optimization case, a desired response with $\tilde{G}_{\mathrm{CRP,max}}^{\mathrm{RF}} = 35$ dBi, $\Delta = 14°$ and $CPSL = -75$ dB is used as shown in (c). The rest of the evaluation parameters are $L_{\mathrm{T}} = L_{\mathrm{R}} = 32$, $L_{\mathrm{T}}^{\mathrm{RF}} = L_{\mathrm{R}}^{\mathrm{RF}} = 1$ and $\mathcal{N}_{\mathrm{freq}} = 2$.

While the CF-C configuration is able to impose explicit RX nulls at selected directions, the proposed CPSL-based beamforming optimization approach goes beyond this and seeks to suppress the overall clutter from different directions outside the sensing beam mainlobe. We next illustrate the power of such approach in the same ABF JCAS scenario, while assume a desired response of $\tilde{G}_{\mathrm{CRP,max}}^{\mathrm{RF}} = 35$ dBi,
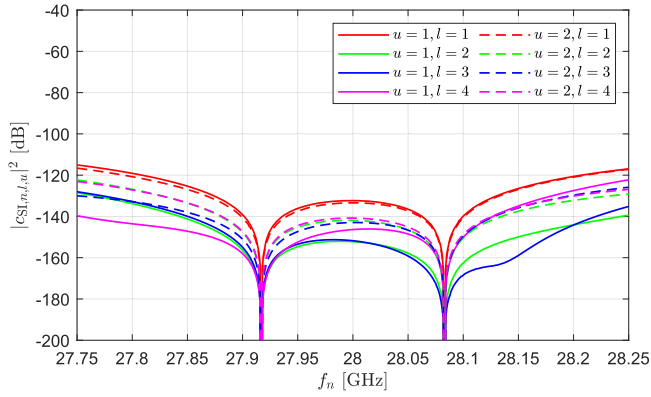
Fig. 6. Illustration of the SI suppression performance in hybrid MU-MIMO JCAS case, showing the effective SI channel between the uth TX stream and the lth RX RF chain. The considered system parameters are: $\theta_{\text{r}} = 10°$, $U = 2$, $\theta_{\text{c},1} = -30°$, $\theta_{\text{c},2} = 30°$, $L_{\text{T}} = L_{\text{R}} = 32$, $L_{\text{T}}^{\text{RF}} = 8$, $L_{\text{R}}^{\text{RF}} = 4$, $\mu_1 = \mu_2 = 15$ dBi, and $\mathcal{N}_{\text{freq}} = 2$.

Fig. 7. Illustration of the SI suppression performance for different numbers of the frequency nulls ($\mathcal{N}_{\text{freq}}$) in the analog array JCAS case using the CF-B configuration. The considered system parameters are: $U = 2$, $\theta_{\text{r}} = 10°$, $\theta_{\text{c},1} = -40°$, $\theta_{\text{c},2} = 40°$ and $L_{\text{T}} = L_{\text{R}} = 32$. The CF-A configuration is used as a reference and corresponds to $\mathcal{N}_{\text{freq}} = 0$.

$\Delta = 14°$ and $CPSL = -75$ dB as shown in Fig. 5(c). As it can be observed, the proposed CPSL optimization which provides more flexibility in the beamforming design, shows the best performance in terms of mitigating or suppressing all possible interference sources outside the sensing mainlobe with a CPSL of around -75 dB. In contrast with the closed-form solution, the main advantage of this approach is the capability of controlling the CPSL for the non-radar directions, and therefore reduce the interference due to the communication beams.

C. Self-Interference Suppression Analysis

We next address and analyze the SI suppression performance that can be achieved through the NSP beamforming solutions. Figure 6 illustrates the obtained SI suppression behavior as a function of frequency in the hybrid MU-MIMO JCAS architecture case when design parameters similar to Fig. 3 are utilized. Here, ideal SI channel estimation capability is yet considered, implying that $\epsilon = 0$. Specifically, the figure illustrates the effective frequency-domain characteristics of the beamformed SI channel in (17) between the uth TX stream and the lth RX RF chain when $\mathcal{N}_{\text{freq}} = 2$ frequency nulls are deployed in the beamforming optimization. As it can be observed, each RX RF chain is subject to different effective SI channels. More concretely, the RX RF chain with $l = 1$ whose subarray is the closest to the TX array exhibits most severe SI coupling. However, overall, the obtained SI suppression numbers are excellent over the whole channel bandwidth.

Figure 7 shows the frequency-domain beamformed SI channel characteristics in the corresponding analog array JCAS architecture case, when design parameters similar to Fig. 5 are used. In this case, we focus on the CF-B beamformer design approach and analyze the effects of the number of frequency nulls, $\mathcal{N}_{\text{freq}}$, on the SI suppression. Additionally, the special case of $\mathcal{N}_{\text{freq}} = 0$ is also shown, corresponding to CF-A, which serves as a reference or baseline. In CF-B design, the frequency nulls are chosen such that they are uniformly distributed within the whole bandwidth,

as $f_{n'} = 27.75 + 0.5\frac{n'}{\mathcal{N}_{\text{freq}}+1}$ GHz with $n' = 1, 2, \ldots, \mathcal{N}_{\text{freq}}$. As can be observed through the results, increasing the number of frequency nulls clearly improves the SI suppression. The case of $\mathcal{N}_{\text{freq}} = 1$ provides an average SI suppression within the considered frequency channel of around -80 dB, while if the number of nulls is increased to $\mathcal{N}_{\text{freq}} = 4$ we can achieve a SI suppression level of around -160 dB already. We note that the baseline level of around -50 dB even when no beamforming based SI suppression is applied ($\mathcal{N}_{\text{freq}} = 0$) stems from the the basic physical isolation between the TX and RX arrays.

We next assess how imperfect SI channel estimates impact the achievable SI suppression performance in the context of the presented beamforming schemes. To this end, Fig. 8 illustrates how the level of the SI channel estimation error, parametrized by ϵ in (37), degrades different system metrics when deploying the alternative beamforming configurations summarized in Table II. As shown in Fig. 8(a), the achievable SI suppression is closely tied with the estimation accuracy. By design, the considered configurations are able to achieve different SI suppression levels depending on the number of nulls when accurate SI channel estimates available. On the other hand, as expected, when the SI channel estimation accuracy decreases, the SI suppression essentially converges to the CF-A configuration ($\mathcal{N}_{\text{freq}} = 0$, only physical isolation), independent of the value of $\mathcal{N}_{\text{freq}}$. It is also noted that the CF-C configuration, which includes additional $\mathcal{N}_{\text{ang}}$ angular nulls to suppress the impact of the communication beams, shows a similar performance compared to the CF-B configuration in terms of SI suppression and its sensitivity to SI channel estimation accuracy.

Furthermore, since errors in the SI channel estimation directly affect the calculation of the NSP matrix in (18), they can also impact the RX beamforming performance. Fig. 8(b) illustrates the potential degradation of the CRP radar gain for different SI channel estimation error levels. Specifically, it can be observed that the number of frequency nulls used for the SI suppression only yields insignificant

(a) Average SI suppression performance

(b) CRP gain
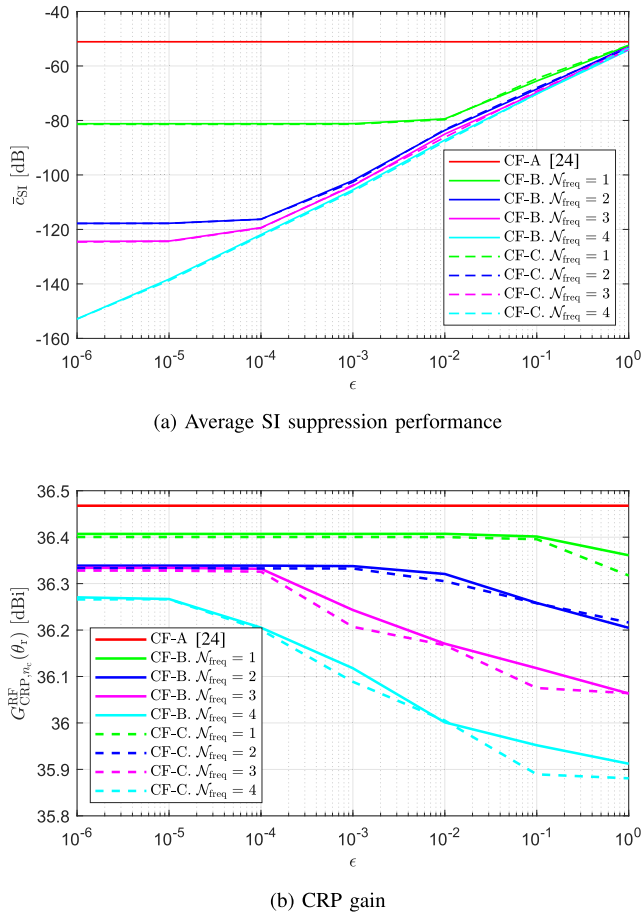
Fig. 8. Illustration of (a) the SI suppression performance and (b) the beamforming performance as functions of the relative SI channel estimation error level, ϵ, in the analog array JCAS case. Also different numbers of the frequency nulls ($\mathcal{N}_{\text{freq}}$) are considered and shown. The main system parameters are: $U = 2$, $\theta_r = 10°$, $\theta_{c,1} = -30°$, $\theta_{c,2} = 30°$ and $L_T = L_R = 32$.

CRP loss of around 0.5 dB, which does not compromise the radar performance of the proposed JCAS system. In addition, if we compare mutually the CF-B and CF-C design approaches, we observe how the angular nulls included in CF-C slightly degrade the CRP gain performance. This performance degradation, due to the loss of beamforming flexibility when applying the presented NSP method, results in a trade-off between the desired SI suppression, CRP gain and the ability to suppress communication beams at the RX side.

D. Representative Sensing Results

Finally, we present example numerical results to validate and assess the actual sensing capability with the different JCAS architectures and proposed beamforming methods, in a scattering environment with 20 static point targets. Ten of these targets are deliberately placed in the direction of the communication beams, at $\theta_{c,1} = -40°$ and $\theta_{c,2} = 40°$, with a radar cross section (RCS) of 10 m^2 as shown in Fig. 9(a). The rest of the targets are uniformly distributed in the sensed area at distances within 10 m to 25 m and angles from $-40°$ to $40°$,

with RCS of 1 m^2. The transmission power is 20 dBm and the thermal noise power in the receiver is -88 dBm. The sensing beam scans the angles between $-60°$ to $60°$ with a step of $1°$. According to [12], we consider an OFDM waveform with $N = 3168$ subcarriers, 10 symbols and $\Delta f = 120$ kHz providing a transmission bandwidth of around 400 MHz. For the actual radar processing to construct the range–angle images, we adopt subcarrier-domain processing that utilizes directly the TX and RX subcarrier samples similar to [20], [31], [32], [33], including also a Hamming window to control the sidelobes. Furthermore, to focus on the impacts of the co-existing communications and sensing beams, we assume for simplicity that ideal SI channel estimates are available.

First, in Fig. 9(b), we illustrate the CF-A beamforming case meaning that no SI nor communication beam suppression is applied. It is noted that in these numerical simulations, we assume sufficiently large RX dynamic range to observe both the target reflections and the strong SI component. However, in practice, this beamforming configuration will easily lead to the saturation of the RX chain, preventing any subsequent sensing functionality. In Fig. 9(b), we can observe how the strong SI appears as a strong close-by target whose sidelobes are spread in the range profiles, masking possible weak targets. Then, the same scenario is assessed with the CF-B beamforming configuration as shown in Fig. 9(c). In this case, the strong SI is suppressed by the NSP method including $\mathcal{N}_{\text{freq}} = 2$ frequency nulls. However, it can be clearly observed that the communication beam interference still generates strong sidelobes, which produce a substantial masking effect along the rest of the sensing directions, thus potentially preventing the detection of weak targets. To overcome this problem, the communication beam is suppressed in the RX side by incorporating angular nulls at the communication directions using the beamforming configuration CF-C, with the corresponding results shown in Fig. 9(d). In this case, the reflections due to the communication beam are suppressed to a certain extent, already improving the sensing capability.

Furthermore, Fig. 9(e) shows the radar image when the proposed CPSL optimization method is implemented. By applying the proposed CPSL optimization based beamforming design, the sidelobe levels can be largely suppressed allowing thus to efficiently avoid such masking problem. As can be observed, the radar image is still clearly improved compared to the different variants of the closed-form method in Figs. 9(b)–(d). Specifically, all the targets are efficiently visible as can be concluded by comparing the subfigures (a) and (e).

Finally, we sense the same scenario with the hybrid MU-MIMO JCAS architecture by using the beamformer design presented in Section III. The corresponding radar image is visually shown in Fig. 9(f). In this case, we utilize a basic radar processing approach, where the received signals at different RX RF chains are combined to maximize the received power at the radar direction while the communication directions are suppressed similar to the CF-C configuration. However, this hybrid architecture, which provides multiple parallel digital signals, will also support more advanced radar processing and related techniques, e.g., multiple signal

(a) Sensing scenario

(b) Analog array, CF-A [24]

(c) Analog array, CF-B

(d) Analog array, CF-C

(e) Analog array, CPSL optimization

(f) Hybrid MU-MIMO
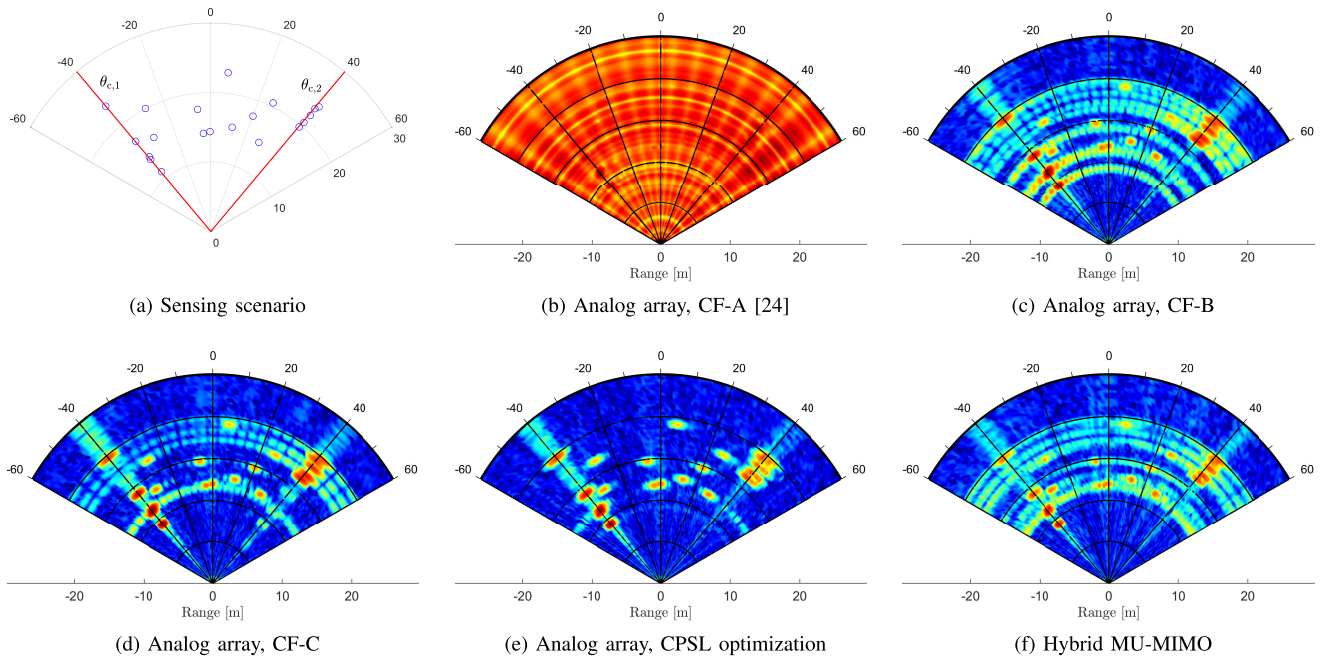
Fig. 9.   In (a), the considered scattering environment with 20 targets and $U = 2$ communication users located at $\theta_{c,1} = -40°$ and $\theta_{c,2} = 40°$ is illustrated. The corresponding sensing results in the analog array JCAS case with different beamforming configurations are shown, as follows: (b) CF-A, (c) CF-B, (d) CF-C and (e) CPSL optimization. Moreover, (f) shows the sensing results using the hybrid MU-MIMO JCAS architecture for the same scenario. For all the considered architectures, the JCAS system senses the environment from $-60°$ to $-60°$ with a step of $1°$.
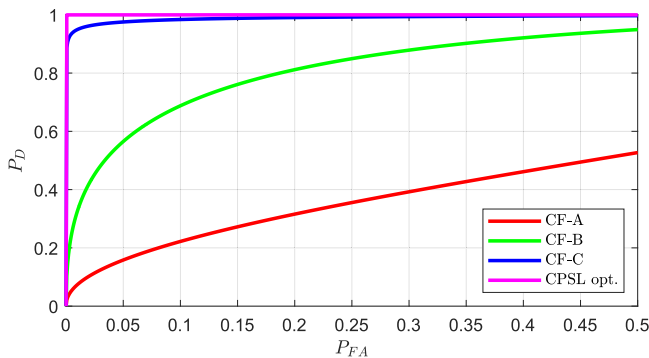
Fig. 10.   Receiver operating characteristic (ROC) performance for the different beamforming schemes, with $\theta_{c,1} = -40°$, $\theta_{c,2} = 40°$, $\theta_r = 20°$, and point targets simultaneously present at all three directions at distances of 10 m.

classification (MUSIC), that will improve the direction of arrival estimation performance [42], [43].

Finally, we investigate the target detection performance of the proposed methods assessing and analyzing the receiver operating characteristic (ROC) curves, shown in Fig. 10. Similar to Fig. 9, the studied scenario considers two communication beams, one at $\theta_{c,1} = -40°$ and another one at $\theta_{c,2} = 40°$, while a sensing beam seeks to illuminate potential targets at $\theta_r = 20°$. Point targets are deliberately placed at all the three directions, all located at distances of 10 m, such that strong interference is induced due to the communications beams. The RCS of all the targets is simulated with a Swerling 2 model. Finally, the ROC curves are obtained by assessing the same scenario for 1000 noise realizations in the following two cases. The first case refers to the null hypothesis with no target being present at the sensing direction, meaning that essentially only

noise and interference are received. The second case refers to the alternative hypothesis, which then also includes the effect of the actual point target at the sensing direction.

As it can be observed in Fig. 10, the worst detection performance corresponds to the CF-A method which does not include any mechanism to suppress the self-interference nor the communication beam masking effects. The detection probability can be improved by suppressing the strong SI through the CF-B scheme with built-in self-interference cancellation. In addition, the performance can be further improved by imposing angular nulls in the communication direction using the CF-C method. Finally, the best performance is obtained by implementing the proposed CPSL optimization approach which simultaneously suppresses the SI and the communication beam interference or masking effect.

VI. Conclusion

In this article, the joint communication and sensing paradigm was addressed and studied, with specific focus on the fundamental challenges with the transmitter–receiver isolation and the co-existing communications and sensing beams in monostatic OFDM radars. We considered both analog beamforming and hybrid analog–digital beamforming based JCAS systems, and proposed multiple new beamformer design and optimization solutions accordingly, addressing the noted challenges with the TX-RX isolation and the co-existing beams. Finally, we analyzed the performance of the proposed methods through extensive numerical experiments with a realistic linear patch array under the effects of non-ideal SI channel estimation, showing that substantial gains and benefits can be achieved with the proposed beamforming and SI cancellation techniques compared to state-of-the-art.

Specifically, in the context of hybrid beamforming based MU-MIMO JCAS systems, we formulated and solved TX and RX beamforming optimization problems that maximize the beamformed power at the sensing direction while constraining the beamformed power at the communications directions, cancel the IUI and suppress the wideband SI by implementing multiple frequency nulls. It was shown that the proposed beamforming scheme is able to cancel the SI leakage without essentially compromising the beamforming performance, viz. CRP loss is insignificant at around 0.5 dB. Additionally, for analog beamforming based JCAS systems, alternative TX and RX beamforming solutions were proposed, which allow the integration of multiple beams for communications and sensing while suppressing the SI. In particular, we observed and showed that the optimization of the combined radar pattern enhances the target detection performance to a great extent, yielding close-to-ideal ROC characteristics in the considered example scenario.

Our future work will include extending the presented work to cover multiple simultaneous sensing beams, to consider independent sensing-related spatial transmit streams in addition to the data streams, and to analyze the impact of different ideal CRP responses. Additionally, actual RF field measurements are pursued in indoor and outdoor scenarios.

References

[1] F. Liu, C. Masouros, A. P. Petropulu, H. Griffiths, and L. Hanzo, "Joint radar and communication design: Applications, state-of-the-art, and the road ahead," *IEEE Trans. Commun.*, vol. 68, no. 6, pp. 3834–3862, Jun. 2020.

[2] C. De Lima et al., "Convergent communication, sensing and localization in 6G systems: An overview of technologies, opportunities and challenges," *IEEE Access*, vol. 9, pp. 26902–26925, 2021.

[3] B. Paul, A. R. Chiriyath, and D. W. Bliss, "Survey of RF communications and sensing convergence research," *IEEE Access*, vol. 5, pp. 252–270, 2017.

[4] K. V. Mishra, M. R. B. Shankar, V. Koivunen, B. Ottersten, and S. A. Vorobyov, "Toward millimeter-wave joint radar communications: A signal processing perspective," *IEEE Signal Process. Mag.*, vol. 36, no. 5, pp. 100–114, Sep. 2019.

[5] A. Hassanien, M. G. Amin, E. Aboutanios, and B. Himed, "Dual-function radar communication systems: A solution to the spectrum congestion problem," *IEEE Signal Process. Mag.*, vol. 36, no. 5, pp. 115–126, Sep. 2019.

[6] C. B. Barneto, S. D. Liyanaarachchi, M. Heino, T. Riihonen, and M. Valkama, "Full duplex radio/radar technology: The enabler for advanced joint communication and sensing," *IEEE Wireless Commun.*, vol. 28, no. 1, pp. 82–88, Feb. 2021.

[7] C. B. Barneto, T. Riihonen, M. Turunen, M. Koivisto, J. Talvitie, and M. Valkama, "Radio-based sensing and indoor mapping with millimeter-wave 5G NR signals," in *Proc. Int. Conf. Localization GNSS (ICL-GNSS)*, Tampere, Finland, Jun. 2020, pp. 1–5.

[8] P. Kumari, J. Choi, N. Gonzalez-Prelcic, and R. W. Heath, Jr., "IEEE 802.11ad-based radar: An approach to joint vehicular communication-radar system," *IEEE Trans. Veh. Technol.*, vol. 67, no. 4, pp. 3012–3027, Apr. 2018.

[9] Q. Huang, H. Chen, and Q. Zhang, "Joint design of sensing and communication systems for smart homes," *IEEE Netw.*, vol. 34, no. 6, pp. 191–197, Nov. 2020.

[10] D. Ma, N. Shlezinger, T. Huang, Y. Liu, and Y. C. Eldar, "Joint radar-communication strategies for autonomous vehicles: Combining two key automotive technologies," *IEEE Signal Process. Mag.*, vol. 37, no. 4, pp. 85–97, Jul. 2020.

[11] D. K. Pin Tan et al., "Integrated sensing and communication in 6G: Motivations, use cases, requirements, challenges and future directions," in *Proc. 1st IEEE Int. Symp. Joint Commun. Sens. (JCS)*, Dresden, Germany, Feb. 2021, pp. 1–6.

[12] *NR; Base Station (BS) Radio Transmission and Reception*, document 3GPP TS 38.104 v15.4.0, Tech. Spec. Group Radio Access Network, Rel. 15, Dec. 2018.

[13] T. Levanen, O. Tervo, K. Pajukoski, M. Renfors, and M. Valkama, "Mobile communications beyond 52.6 GHz: Waveforms, numerology, and phase noise challenge," *IEEE Wireless Commun.*, vol. 28, no. 1, pp. 128–135, Feb. 2021.

[14] U. Gustavsson et al., "Implementation challenges and opportunities in beyond-5G and 6G communication," *IEEE J. Microw.*, vol. 1, no. 1, pp. 86–100, Jan. 2021.

[15] C. B. Barneto et al., "High-accuracy radio sensing in 5G new radio networks: Prospects and self-interference challenge," in *Proc. 53rd Asilomar Conf. Signals, Syst., Comput.*, Pacific Grove, CA, USA, Nov. 2019, pp. 1159–1163.

[16] S. Kutty and D. Sen, "Beamforming for millimeter wave communications: An inclusive survey," *IEEE Commun. Surveys Tuts.*, vol. 18, no. 2, pp. 949–973, 2nd Quart., 2016.

[17] R. W. Heath Jr., N. González-Prelcic, S. Rangan, W. Roh, and A. M. Sayeed, "An overview of signal processing techniques for millimeter wave MIMO systems," *IEEE J. Sel. Topics Signal Process.*, vol. 10, no. 3, pp. 436–453, Apr. 2016.

[18] M. L. Rahman, J. A. Zhang, X. Huang, Y. J. Guo, and R. W. Heath Jr., "Framework for a perceptive mobile network using joint communication and radar sensing," *IEEE Trans. Aerosp. Electron. Syst.*, vol. 56, no. 3, pp. 1926–1941, Jun. 2020.

[19] J. A. Zhang et al., "Enabling joint communication and radar sensing in mobile networks—A survey," 2020, *arXiv:2006.07559*.

[20] C. B. Barneto et al., "Full-duplex OFDM radar with LTE and 5G NR waveforms: Challenges, solutions, and measurements," *IEEE Trans. Microw. Theory Techn.*, vol. 67, no. 10, pp. 4042–4054, Oct. 2019.

[21] F. Guidi, A. Guerra, and D. Dardari, "Personal mobile radars with millimeter-wave massive arrays for indoor mapping," *IEEE Trans. Mobile Comput.*, vol. 15, no. 6, pp. 1471–1484, Jun. 2016.

[22] S. D. Liyanaarachchi, T. Riihonen, C. B. Barneto, and M. Valkama, "Optimized waveforms for 5G–6G communication with sensing: Theory, simulations and experiments," *IEEE Trans. Wireless Commun.*, vol. 20, no. 12, pp. 8301–8315, Dec. 2021.

[23] W. Roh et al., "Millimeter-wave beamforming as an enabling technology for 5G cellular communications: Theoretical feasibility and prototype results," *IEEE Commun. Mag.*, vol. 52, no. 2, pp. 106–113, Feb. 2014.

[24] J. A. Zhang, X. Huang, Y. J. Guo, J. Yuan, and R. W. Heath, Jr., "Multibeam for joint communication and radar sensing using steerable analog antenna arrays," *IEEE Trans. Veh. Technol.*, vol. 68, no. 1, pp. 671–685, Jan. 2019.

[25] Y. Luo, J. A. Zhang, X. Huang, W. Ni, and J. Pan, "Multibeam optimization for joint communication and radio sensing using analog antenna arrays," *IEEE Trans. Veh. Technol.*, vol. 69, no. 10, pp. 11000–11013, Oct. 2020.

[26] X. Liu, T. Huang, N. Shlezinger, Y. Liu, J. Zhou, and Y. C. Eldar, "Joint transmit beamforming for multiuser MIMO communications and MIMO radar," *IEEE Trans. Signal Process.*, vol. 68, pp. 3929–3944, 2020.

[27] Y. Luo, J. A. Zhang, X. Huang, W. Ni, and J. Pan, "Optimization and quantization of multibeam beamforming vector for joint communication and radio sensing," *IEEE Trans. Commun.*, vol. 67, no. 9, pp. 6468–6482, Sep. 2019.

[28] J. Guan, A. Paidimarri, A. Valdes-Garcia, and B. Sadhu, "3-D imaging using millimeter-wave 5G signal reflections," *IEEE Trans. Microw. Theory Techn.*, vol. 69, no. 6, pp. 2936–2948, Jun. 2021.

[29] A. Sabharwal, P. Schniter, D. Guo, D. W. Bliss, S. Rangarajan, and R. Wichman, "In-band full-duplex wireless: Challenges and opportunities," *IEEE J. Sel. Areas Commun.*, vol. 32, no. 9, pp. 1637–1652, Sep. 2014.

[30] K. E. Kolodziej, B. T. Perry, and J. S. Herd, "In-band full-duplex technology: Techniques and systems survey," *IEEE Trans. Microw. Theory Techn.*, vol. 67, no. 7, pp. 3025–3041, Jul. 2019.

[31] M. Braun, "OFDM radar algorithms in mobile communication networks," Ph.D. dissertation, Commun. Eng. Lab (CEL), Karlsruhe Institut für Technologie (KIT), Germany, 2014.

[32] C. Sturm, E. Pancera, T. Zwick, and W. Wiesbeck, "A novel approach to OFDM radar processing," in *Proc. IEEE Radar Conf.*, Pasadena, CA, USA, May 2009, pp. 1–4.

[33] C. Sturm, T. Zwick, and W. Wiesbeck, "An OFDM system concept for joint radar and communications operations," in *Proc. IEEE 69th Veh. Technol. Conf.*, Barcelona, Spain, Apr. 2009, pp. 1–5.

[34] I. T. Cummings, J. P. Doane, T. J. Schulz, and T. C. Havens, "Aperture-level simultaneous transmit and receive with digital phased arrays," *IEEE Trans. Signal Process.*, vol. 68, pp. 1243–1258, 2020.

[35] S. A. Hassani et al., "In-band full-duplex radar-communication system," *IEEE Syst. J.*, vol. 15, no. 1, pp. 1086–1097, Mar. 2020.

[36] H. Zhu and J. Wang, "Chunk-based resource allocation in OFDMA systems—Part I: Chunk allocation," *IEEE Trans. Commun.*, vol. 57, no. 9, pp. 2734–2744, Sep. 2009.

[37] C. B. Barneto, S. D. Liyanaarachchi, T. Riihonen, L. Anttila, and M. Valkama, "Multibeam design for joint communication and sensing in 5G new radio networks," in *Proc. IEEE Int. Conf. Commun. (ICC)*, Dublin, Ireland, Jun. 2020, pp. 1–6.

[38] S. Banerjee and A. Roy, *Linear Algebra and Matrix Analysis for Statistics* (Chapman & Hall/CRC Texts in Statistical Science). USA: Taylor & Francis, 2014.

[39] T. Riihonen, S. Werner, and R. Wichman, "Mitigation of loopback self-interference in full-duplex MIMO relays," *IEEE Trans. Signal Process.*, vol. 59, no. 12, pp. 5983–5993, Dec. 2011.

[40] C. B. Barneto, S. D. Liyanaarachchi, T. Riihonen, M. Heino, L. Anttila, and M. Valkama, "Beamforming and waveform optimization for OFDM-based joint communications and sensing at mm-waves," in *Proc. 54th Asilomar Conf. Signals, Syst., Comput.*, Pacific Grove, CA, USA, Nov. 2020, pp. 895–899.

[41] F. Liu, C. Masouros, A. Li, H. Sun, and L. Hanzo, "MU-MIMO communications with MIMO radar: From co-existence to joint transmission," *IEEE Trans. Wireless Commun.*, vol. 17, no. 4, pp. 2755–2770, Apr. 2018.

[42] Y. Leen Sit, C. Sturm, J. Baier, and T. Zwick, "Direction of arrival estimation using the MUSIC algorithm for a MIMO OFDM radar," in *Proc. IEEE Radar Conf.*, Atlanta, GA, USA, May 2012, pp. 0226–0229.

[43] S. D. Liyanaarachchi, C. B. Barneto, T. Riihonen, M. Heino, and M. Valkama, "Joint multi-user communication and MIMO radar through full-duplex hybrid beamforming," in *Proc. 1st IEEE Int. Online Symp. Joint Commun. Sens. (JCS)*, Dresden, Germany, Feb. 2021, pp. 1–5.

Sahan Damith Liyanaarachchi (Graduate Student Member, IEEE) received the B.Sc. degree (Hons.) from the University of Peradeniya, Sri Lanka, in 2016, and the M.Sc. degree (Hons.) from Tampere University, Finland, in 2019, where he is currently pursuing the doctoral degree with the Unit of Electrical Engineering. His research interests include waveform optimization for joint communication and sensing systems, and evolution of beyond 5G systems.

Mikko Heino (Member, IEEE) received the D.Sc. degree in radio engineering from Aalto University, Helsinki, in 2020. He is a Post-Doctoral Research Fellow with the Unit of Electrical Engineering, Tampere University, Finland. His research interests include joint communication and sensing systems, antenna isolation improvement methods for in-band full-duplex systems, and millimeter wave antenna design and user effect characterization.

Nuria González-Prelcic (Senior Member, IEEE) received the Ph.D. degree in electrical engineering from the University of Vigo, Spain, in 2000. She was an Associate Professor at the Signal Theory and Communications Department, the University of Vigo, and also held visiting positions at the University of Texas at Austin and the University of New Mexico. She was also the Founding Director of the Atlantic Research Center for Information and Communication Technologies (atlanTTic) at the University of Vigo from 2008 to 2017. She joined as an Associate Professor with the Faculty of NC State, in 2020. Her main research interests include signal processing theory and signal processing and machine learning for wireless communications: filter banks, compressive sampling and estimation, multicarrier modulation, massive MIMO, MIMO processing for millimeter-wave communication, including vehicle-to-everything (V2X), air-to-everything (A2X) and LEO satellite communication. She is also interested in joint localization and communication, joint radar and communication, and sensor assisted communication. She is an elected member of the IEEE Sensor Array and Multichannel Technical Committee and the IEEE Signal Processing for Communications and Networking Technical Committee. She is a member of the IEEE SPS Integrated Sensing and Communication Technical Working Group. She has published more than 120 papers in the topic of signal processing for millimeter-wave communications, including a highly cited tutorial published in the IEEE JOURNAL OF SELECTED TOPICS IN SIGNAL PROCESSING which has received the 2020 IEEE SPS Donald G. Fink Overview Paper Award and an article pioneering the idea of using mmWave WiFi signals for automotive radar that won the IEEE Vehicular Technology Society 2022 Best Vehicular Electronics Paper Award. She is an Editor of IEEE TRANSACTIONS ON COMMUNICATIONS.

Carlos Baquero Barneto (Student Member, IEEE) received the B.Sc. and M.Sc. degrees in telecommunication engineering from Universidad Politécnica de Madrid, Spain, in 2017 and 2018, respectively, and the D.Sc. degree from Tampere University, Finland. His research interests include joint communication and sensing systems' design, with particular emphasis on 5G and beyond mobile radio networks.

Taneli Riihonen (Senior Member, IEEE) received the D.Sc. degree (Hons.) in electrical engineering from Aalto University, Helsinki, Finland, in 2014. He is currently a Tenure-Track Associate Professor with the Faculty of Information Technology and Communication Sciences, Tampere University, Finland. His research interests include physical-layer OFDM(A), multiantenna, and multihop and full-duplex wireless techniques with current interest in the evolution of beyond 5G systems.

Mikko Valkama (Fellow, IEEE) received the M.Sc.(Tech.) and D.Sc.(Tech.) degrees (Hons.) from the former Tampere University of Technology in 2000 and 2001, respectively. In 2003, he was with San Diego State University (SDSU), CA, USA, as a Visiting Postdoctoral Fellow. Currently, he is a Full Professor and the Head of the Unit of Electrical Engineering with the newly formed Tampere University (TAU), Finland. His general research interests include radio communications, radio localization, and radio-based sensing, with particular emphasis on 5G and 6G mobile radio networks.